YIELDING AND FRACTURE IN NANOLAYERED METALLIC COMPOSITES

By
NICOLE REBECCA OVERMAN

A dissertation in partial fulfillment of the requirements for the degree of
MASTER OF SCIENCE IN MATERIALS SCIENCE AND ENGINEERING

WASHINGTON STATE UNIVERSITY
School of Mechanical and Materials Engineering

August 2009

To the faculty of Washington State University:

The members of the Committee appointed to examine the dissertation of NICOLE REBECCA OVERMAN find it satisfactory and recommend that it be accepted.

David F. Bahr, Ph. D., Chair

Hussein M. Zbib, Ph. D.

David P. Field, Ph. D.

ACKNOWLEDGMENTS

I would like to acknowledge and thank my advisor, Dr. Bahr for his continued support and guidance throughout this process. I appreciate his contributions and encouragement throughout my research. I would also like to thank the members of my committee, Dr. Hussein Zbib and Dr. David Field for their advice and willingness to help. Additionally, I would like to thank John Vetrano for financial support of this project and Los Alamos National Labs for fabrication of the multilayer films.

There are also several staff members, students and faculty which have repeatedly been an immense help to me, providing time, knowledge and guidance to me whenever it was needed. I would like to thank Aikaterini Bellou for her help with the SEM and nanoindenter. Thanks to John Yeager, Joshah Jennings and John Youngsman for the time they spent helping me in the cleanroom. I am also grateful to Annette Cavalieri, Jan Danforth and Bob Ames for their support.

My biggest thanks go to my husband Cory for his support and understanding throughout this process, I could not have done it without him.

YIELDING AND FRACTURE IN NANOLAYERED METALLIC COMPOSITES

ABSTRACT

by Nicole Rebecca Overman, MS
Washington State University
August 2009

Chair: David F. Bahr

Thin films are currently being used in virtually all forms of electronic devices, as protective coatings, MEMS and even some drug delivery systems. In many cases the strength of films becomes a critical factor in their reliability. For this reason, a better understanding of their mechanical properties is needed. Multilayer metallic films in particular exhibit higher strengths than the constituents alone.

This work utilized bulge testing in conjunction with nanoindentation to study the elastic properties, the onset of yielding, and eventual failure of several multilayered film systems and geometries. CuNb, CuNi and CuNbNi multilayers with individual layer thicknesses of 20nm were studied. Though the CuNi films had extremely poor adhesion strength, these films had the highest pressures needed to cause fracture , reaching values approximately 1/3 higher than the CuNb and CuNbNi films. However, the CuNb films were shown to exhibit higher hardnesses than the CuNi and CuNbNi films. These differences were attributed to a difference in the strain hardening abilities of these films. The information found from this work will serve to be the base line for fatigue testing of these films in the future.

TABLE OF CONTENTS

TABLE OF FIGURES

LIST OF TABLES

Chapter One: Introduction

1.1 Background

In accordance with Moore's Law, the number of transistors on a computer chip doubles every 18 months, increasing the processing speed and memory capacity. This trend, first observed by Intel's cofounder, Gordon Moore in his famous 1965 paper "Cramming more components onto integrated circuits" [1] has proven itself for nearly the past fifty years, relying on the ability to make these components smaller and smaller. With the semiconductor industry, no doubt the most booming hardware industry of the past few decades[2] driving the feature dimensions on electromechanical and thin film devices to the nanometer scale.

To achieve such miniaturized devices, thin film technologies such as photolithography, sputtering and advanced materials, have been the key areas of tremendous development in the field of microelectronics. Advances in photolithography achieve narrower line widths and finer detail by moving to shorter and shorter wavelengths of light for photoresist development. Materials advancements in these small devices has also encountered significant development. In the past 30 years, interconnects have evolved from single layer Al, deposited by evaporation, to multiple levels of sandwiched Ti/Al–Cu/TiN metal layers deposited by sophisticated magnetron sputtering and connected by aluminum or tungsten vias.[3]

With the production and development of multilayered thin films, a new area of nano-layered composites research was developed. As noted in the literature, layer by layer assembly method provides significant flexibility to a designer of materials. [4] Layer materials,

thickness, substrate material, roughness, texture and interfaces could all be tailored or modified to achieve desired properties.

1.2 Motivation

Understanding the mechanical properties of thin films has attracted attention due to the important role these films play in microsensors, actuators, and almost all the "high tech" devices used on a day to day basis. Applications of thin films cover a broad range of topics including fuel cells, solar technology, flexible electronics, and even sunglasses. According to a report, released by BBC Research in 2008, the projected global market for thin films is showing tremendous growth, with Figure 1.1 showing the growth potential of these materials over the next five years.[5]

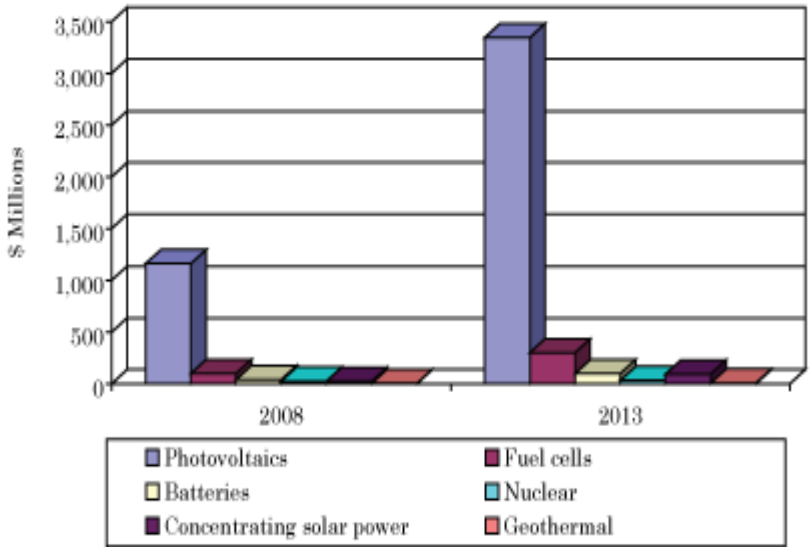

Figure 1.1 – The projected global market for thin films is shown to triple in the next 5 years, reaching a total of 3.2 billion dollars.[5]

Because thin films used in these applications often have thicknesses on the same characteristic length scale as their microstructure,[6] the mechanical behavior will be significantly different then their bulk counterparts. Several studies on copper based multilayers performed by Misra and Wang, among others,[7,8,9] have shown yield strengths in excess of 2 GPa at layer thicknesses of a few nanometers, significantly higher than that of bulk Cu and Niobium at 10-50 MPa. These multilayers can be "stacked" to form materials to fractions of mm's in thickness. These values for thin film CuNb, as seen in Figure 1.2, have strength values approaching the theoretical limit.[10]

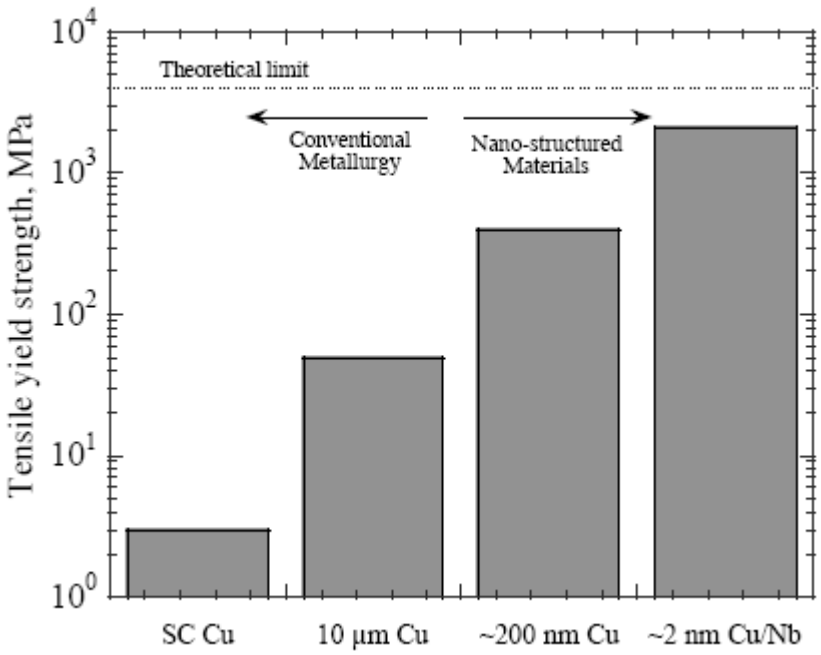

Figure 1.2 – Nano-structured and layered devices exhibit strength far beyond that of bulk and thick films.[10]

Because of their enhanced properties thin films have become very popular, and this popularity has led them to be used in a tremendous variety of applications. However, almost

every application these films are utilized in requires them to withstand some sort of stress or strain. For this reason, a better understanding the mechanical behavior of these thin film systems is necessary to identify their mechanical and interfacial limitations. Understanding these limitations is the first step towards developing enhanced and more reliable products.

The goal of this project was to mechanically characterize multilayer thin film systems, primarily Copper/Niobium, Copper/Nickel, and Copper/Nickel/Niobium. Because these may be used in devices that experience frequent cyclic loading conditions, both thermally and mechanically which occur as devices are switched off and on, dropped, charged and exposed to the elements, understanding their fatigue behavior is extremely important. However, in order to perform fatigue testing on these films at the appropriate stresses and strains, it is first necessary to develop an understanding of the aspects of plastic deformation and failure which occur in these films at quasi-static conditions. To achieve this goal, several thin film testing methods were employed, including: nanoindentation, bulge testing, burst testing and scanning electron microscopy. A variety of stress states were incorporated into this study by testing several different window geometries with a variety of stress concentrations.

1.3 Thin Film Properties

1.3.1 Thin Film Growth Kinetics

In general, kinetic considerations that should be addressed are those that affect the surface structure evolution. For the purposes of this thesis, thin film formation begins by vapor deposition. Atoms leave the vapor phase and land on the surface, moving around to form clusters. The likely growth method for these systems is Volmer-Weber or island growth, in this model, nuclei grow as islands in the shape of a spherical cap with isotropic surface

energies.[11] During deposition, the flux of atoms arriving at the surface (Q) will remain adsorbed for a mean residence time, τ. Nucleation forms when stable clusters of adatoms form and continue to grow rather than dissolving back to smaller clusters or adatoms. Based on an atomistic analysis[11] the nucleation rate can be described as:

$$R = I_o Q^{n^*} \exp\left(\frac{-\Delta G_{n^*}}{kT}\right) \tag{1.1}$$

where I_o is a constant, k is Boltzman's constant, T is the substrate temperature, ΔG_{n^*} is the energy of formation for a cluster of critical size n^*. When cluster sizes become sufficiently large, crystallographic orientation plays a role in the sense that certain orientations can reduce the energies associated with nucleating islands so that nucleation of specific orientations is favored, a similar process occurs with coarsening.

Because surface and interface energies are dependent on the orientation of the lattice with respect to the island, energy differences which drive coarsening processes depend not only on island orientation but also on its size relative to neighboring islands.[11] Coarsening can then occur by detachment and diffusion of atoms from islands over the substrate to nearby islands. The net effect of this is the shrinkage and disappearance of high energy islands and the growth of low energy islands. Therefore, the energetics of grain structure evolution in thin films on substrates are affected by the surface energy γ_s, the interfacial energy γ_i, and the strain energy density, all of which vary with the crystallographic orientation of a grain.[11]

1.3.2 Residual Stresses

Residual stresses occur in a variety of thin film systems and are almost impossible to completely eliminate. Understanding and identification of the magnitude of these stresses is necessary because of their deleterious effects on the reliability of thin film systems by fatigue, aging or film delamination. Of these three, delamination has proved to be one of the most challenging issues encountered during testing for the current study. In addition, thin films used for semiconductor and mechanical applications have shown the residual stress is an important factor which has an influence on hardness, toughness and thin film adhesion to the substrate.[12,13]

There are three well established forms of residual stress in thin films: epitaxial stresses, thermal stresses, and intrinsic or growth stresses. While the primary area of focus as applied to the experimental results will be on epitaxial and intrinsic stresses, all three types are briefly discussed in this section.

EPITAXIAL STRESSES

Epitaxial stresses occur as a direct result of a mismatch in the lattice spacing between the film and substrate. However, this effect is limited to the first few atomic layers which are deposited. As the film grows and continues to increase in thickness the effects of these stresses are relieved by the formation of misfit dislocations[14] as seen in Figure 1.3[15]. For the case of multilayer films where interfaces are abundant, epitaxial stresses have gained a significant amount of attention when determining critical layer thicknesses required for the formation of misfit dislocations. Further discussion on these size effects and length scales in multilayer films can be found in section 1.3.4.

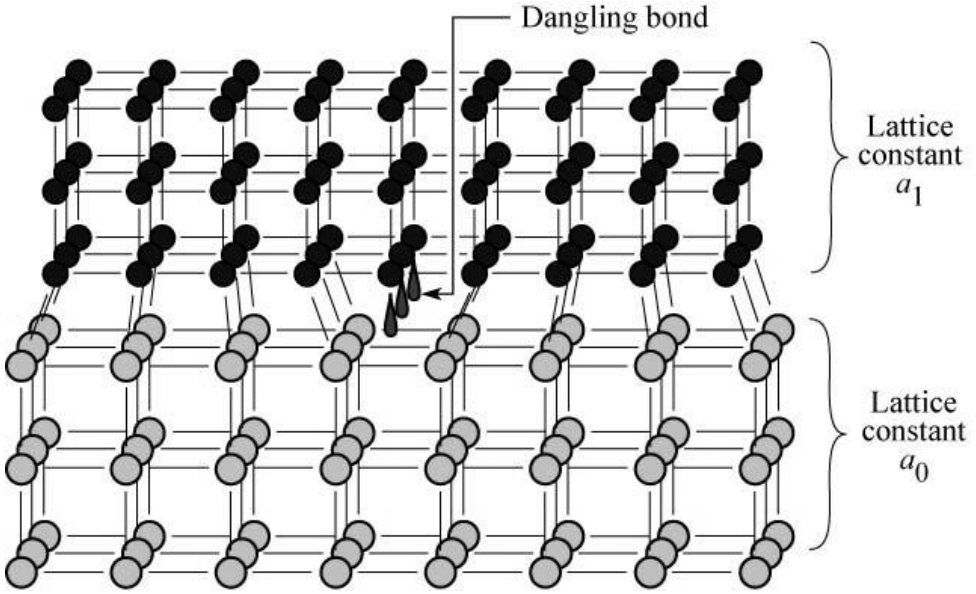

Figure 1.3 – Differences in lattice parameter result in localized distortions which result in epitaxial stresses at the boundary.[15] These stresses are relieved by dislocation formation.

THERMAL STRESSES

Thermal stresses come about due to a mismatch in the coefficient of thermal expansion between the film and substrate, for multilayer films they can also occur between the layers. For the case of the film/substrate system a large CTE mismatch would occur as it cools to room temperature after deposition. For example, in the case where the CTE of the substrate is higher than that of the film, this would result in a compressively stressed film if the growth occurs in a stress free condition. In the case of the multilayer systems of interest, thermal stresses are not aniticipated to have much of an impact. Copper and Nickel for example were anticipated to form a strong couple because of the similarity in the crystal structures and the room temperature lattice parameters are very similar and their coefficients of thermal expansion are reasonably close at 17.8 x10^{-}6 (Cu) and 13.97x10^{-6} (Ni).[16]

INTRINSIC STRESSES

The development of growth or intrinsic stresses begins during the deposition process. Not to be confused with the previously discussed stresses, intrinsic stresses are solely a product of film growth. There several reported sources of intrinsic stresses in thin films including: small angle grain boundaries, domain walls, recrystallization processes, impurities, capillary stresses or by a lattice expansion mechanism.[17,18] Of these, probably the most widely used explanations applied to epitaxially grown columnar films are those of small angle grain boundaries and domain walls; researchers have assumed that tensile stresses occur due to small angle grain boundaries and compressive stresses are due to domain walls. [17]

Polycrystalline, columnar thin films usually exhibit a high concentration of low angle grain boundaries. In classical models these boundaries have been thought of as a primary cause of intrinsic stresses in the film. Interatomic attractive forces working to close the boundaries lead to a film with a tensile stress state. [17]While this is not always true, because not all boundaries are strained, on average intrinsic tensile stresses in thin films are caused by small angle grain boundaries.[17-19]

Also common to thin films are compressive stress states. During Volmer-Weber growth, because the islands have the same out of plane orientation (with respect to the substrate) but are free to nucleate anywhere, it is highly unlikely that the lattices of coalescing islands will be oriented identically in the substrate plane (x and y directions). "The boundaries which are then created are referred to as domain walls, and are typically found to be compressively stressed." [17]

1.3.3 Film Structure

Initially nucleated film grains provide the template that often results in a fully developed grain structure,[20] and as discussed previously, for epitaxially grown films, the substrate plays a significant role at the start of deposition. This influence comes from the misfit and thermal stress, defects at the crystal-film interface, and from chemical interactions between the film and substrate.[21]

The influence deposition variables have on the structural features that develop in physically deposited films has been a universally studied topic, and has resulted in the development of structure-zone diagrams[20] (SZDs). The multilayer films studied in this thesis were deposited by DC magnetron sputtering. The diagram shown in Figure 1.4 depicts the widely popular Thornton SZD for a sputtered film.

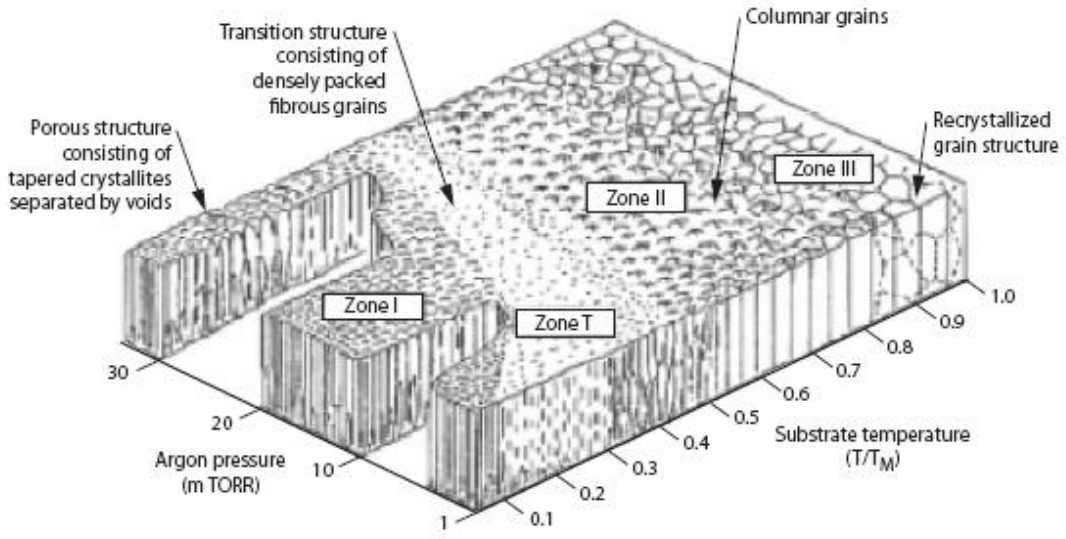

Figure 1.4 - Thorton's Structure Zone Diagram[20] describes the effect of temperature and pressure on the sputtered film; porous, columnar, recrystallized and transition structures are visible.

As seen in the diagram, substrate temperature and processing pressure are key variables during sputter deposition that influence the final film structure. As a thin film is deposited, there are several competing factors which occur including: surface diffusion, bulk diffusion, shadowing and desorption. These processes are responsible for creating the different zones, and are all thermodynamically controlled via substrate temperature. To better understand the effect pressure has, it is useful to consider this axis in terms of energy. In this sense, a lower pressure can be thought of has having high kinetic energy, with the opposite being true for high pressures. In this sense, low pressure deposition leads to increased energetic atom bombardment which densifies the film.[20]

The multilayer films of interest to this work are zone II films, polycrystalline with individual layers composed of columnar grains. The individual layer thickness for each of the film systems in this study was 20nm. Therefore, because of the number of interfaces present it should be noted that by alternating the deposition of copper, nickel and niobium, phenomena like nucleation, growth and coalescence of nuclei takes place at every interface restarting the complete thin film growth process. In this way, the grain shape and columnar structure of the individual layers define the starting surface for the formation of morphological features in the following layers of the multilayer system.[22]

It should also be mentioned that while the SZD shown is commonly accepted, several modifications have been made for specific cases. For example, for magnetron sputtered Al_2O_3 the major variable in this SZD is oxygen content, which described in [20] becomes a complex function of both the electrical and chemical reactions occurring in the plasma.

1.3.4 Length Scale & Size Effects

Size effects in polycrystalline materials have historically been modeled using the famous Hall-Petch relation;

$$\sigma_y = \sigma_0 + \frac{k_y}{\sqrt{d}} \tag{1.2}$$

where the material strength is dependent upon *d*, the grain size diameter and *k*, a material specific strengthening constant. Recently, size effects in metallic composites have been an area of interest because, while plastic deformation of coarse grained materials at temperatures below .4Tm is accommodated by the nucleation and motion of dislocations; at very small grain sizes dislocation sources and pile-ups are not expected to exist.[23]

The idea of a breakdown in the Hall Petch effect (strengthening of a material by grain refinement) has been proposed and modeled by several researchers.[23-32] As crystal planes shear, dislocations interact with each other and stress concentrations as they pile up at the grain boundaries. "Because pileups in fine-grained materials contain fewer dislocations, larger stresses are required to generate dislocations in neighboring grains. This is also an effect of the decreased stress at the tip of the pileup.[24]The distance between dislocation pinning points is greatly reduced which requires very high stresses for them to be activated. In addition it has been shown that the number of glide systems active does not reach the five required for deformation in polycrystals.[32] So, the main problem in assigning Hall Petch dependence ($\sigma_y \propto d^{-1/2}$) to nanocrystalline materials is that this model is only valid at grain sizes where dislocation pileups can occur. The mechanism breaks down at smaller grain sizes

because grains are unable to support dislocation pile-ups, and the Hall Petch dependence is no longer accurate, [23,25,26,27] to the extent that softening has been observed with decreasing grain size in specimens of copper, nickel, zinc and palladium with initial grain sizes in the nanometer range.[23,24,27,28,29,30]

However, for multilayer film systems, the layer thickness also has to be considered to develop a complete understanding of the properties of these film systems. To address these issues, a schematic illustration of the operative dislocation mechanisms of multilayer thin films has been developed by Hirth. Figure 1.5 shows the proposed dislocation activity present for different layer thicknesses.[7]

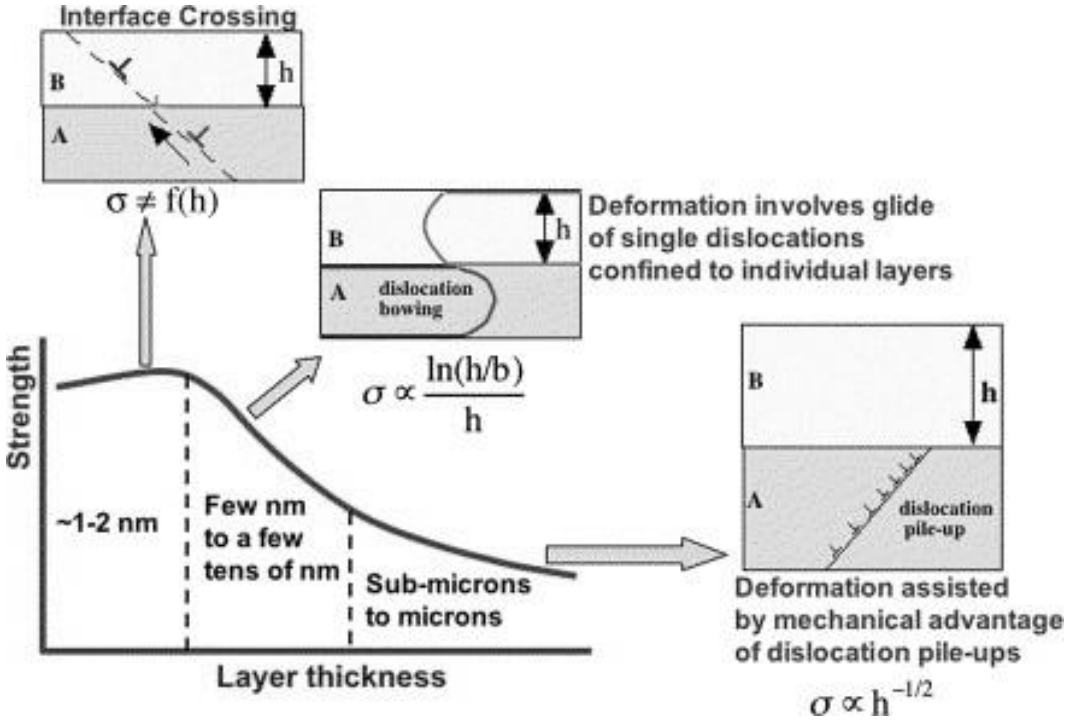

Figure 1.5 – Three distinct deformation mechanisms are present and controlled by layer thickness. As layer thickness decreases, the Hall Petch regime breaks down, allowing for the strengths seen in multilayer and thin film systems.[7]

For the 20nm layer thicknesses of all the film systems in this study, deformation should occur predominantly by glide of single dislocations confined within each layer.

1.4 Overview

This thesis is divided into three major sections:

- Chapter 2 provides details regarding the experimental methods which were used. Techniques and principals are discussed for: photolithography, reactive ion etching, laser interferometry, bulge and burst testing, nanoindentation and microscopy.
- Chapter 3 describes the initial yielding conditions in CuNb, CuNi and CuNbNi multilayer systems for a variety of membrane geometries.
- Chapter 4 includes a discussion of multilayer failures via burst testing and compares this to failures seen in single layer copper films. Information on the maximum stresses and strains observed is also presented.

1.5 References

[1] Moore, G. "Cramming more components onto integrated circuits," 1965 Electronics, **38**(8).

[2] Sauter, W. "Thin Film Mechanics Bulging and Stretching," 2002, PhD Thesis, University of Vermont, USA.

[3] Liu, R., Pai, C.S., Martinez, E., "Interconnect technology trend for microelectronics," 1999, Solid-State Electronics, **43**(6), pp. 1003-1009

[4] Gero Decher, Joseph B. Schlenoff Multilayer Thin Films – Sequential Assembly of Nanocomposite Materials. Wiley & Sons 2003

[5] Moran, B. "Global Market for Thin Films in Energy Applications," (2008) Online accessed at www.bccresearch.com, pp.1-174

[6] Eijden, R.V. "Numerical-experimental analysis of an improved bulge test for thin films," 2008, Masters Thesis, Eindhoven University of Technology, Netherlands.

[7] Misra, A., Demkowiex, M.J., Wang, J., Hoagland, R.G., (2008) "The Multiscale Modeling of Plastic Deformation in Metallic Nanolayered Composites," JOM, **60**(4) pp.39-42

[8] Tokarz, A., Fraczek, T., Balaga, Z., Nitkiewicz, Z., "Structure, Hardness, and Thermal Stability of Electrodeposited Cu/Ni Nanostructured Multilayers," (2007) Rev. Adv. Mater.Sci, **15**, pp. 247-252

[9] Misra, A., Zhang, X., Hammon, D., Hoaglane, R.G., "Work hardening in rolled nanolayered metallic composites," (2005) Acta Mat. **53**, pp. 221-226

[10] Wang, Y.C., "Mechanical fatigue properties of self-supported nano-layered Composites," Online accessed: www.stam.org, pp.1-15

[11] Thompson, C.V., "*Structure evolution during processing of polycrystalline films*," (2000) Annu. Rev. Mater. Sci. **30** pp.159–190

[12] Wantanabe, Y., Kitazawa, N., Nakamura, Y. "Mechanical properties and residual stress in AlN films prepared by ion beam assisted deposition," (2000) J. Vac. Sci. Technology 18(4) 1567-1570

[13] Keckes, J., Six,S., Tesch,W., Resel, R., Rauschenbach, B., "Evaluation of thermal and growth stresses in heteroepitaxial AlN thin films formed on (0 0 0 1) sapphire by pulsed laser ablation," (2002) J. Crystal Growth, **240**(1-2), pp. 80-86

[14] Matthews, J.W., Blakeslee, A.E., "Defects in epitaxial multilayers. I. Misfit dislocations" (1974) J.Cryst. Growth

[15] Scheubert, E.F., "Light Emitting Diodes" Cambridge Univ. Press 2006

[16] Koehler, J.S., "Attempt to design a Strong Solid" (1970) Physical Review B 2(2) pp.547-551

[17] Koch, R. "The intrinsic stress of polycrystalline and epitaxial thin metal films" (1994) J. Phys.: Condens. Matter **6** pp. 9519-9550.

[18] Freund, L.B., Suresh, S.*"Thin Film Materials: Stress, Defect Formation, and Surface Evolution."*Cambridge Univ. Press, 2003.

[19] Hoffman, R.W., Hass, G., Thun, R.E., "Influence of Substrate Properties on the Growth of Titanium Films, Part I," (1966) Physics of Thin Solid Films, **3**, pp. 211.

[20] Ohring, M., "Materials Science of Thin Films" Academic Press, 2002.

[21] Herman, M.A., Richter, W., Sitter, H., "Epitaxy: Physical Principals and Technical Implementation" Springer, 2004.

[22] Czigány, Z., Radnóczi, G., Columnar growth structure and evolution of wavy interface morphology in amorphous and polycrystalline multilayered thin films," (1999) Thin Solid Films **347**(1-2), pp.133-145.

[23] Shan,Z., Stach,E., Weizorek,J., Knapp,J., Follstaedt,D., Mao,S., "Grain Boundary Mediated Plasticity in Nanocrystalline Nickel,"(2004) Sci.Mag, **305**, pp.654-657

[24] Conrad, H., "Narayan, J., Mechanism for grain size softening in nanocrystalline Zn," (2002) Appl. Phys. Letters, **81**, pp.2241

[25] Yip, Sidney. "The Strongest Size," (1998) Nature, **391,** pp.532-533

[26] Ma, E. "Watching the Nanograins Roll," (2004) Sci.Mag., **305**, pp.623-624

[27] Carlton, C.E., Ferreira, P.J., "What is behind the inverse Hall-Petch effect in nanocrystalline materials," (2007) Acta Materilia, **55,** pp.3749-3756

[28] Nieh, T.G., Wang, J.G., "Hall Petch relationship in nanocrystalline Ni and Be-B alloys," (2005) Intermetallics, **13**(3-4), pp.377-385

[29] Schuh, C.A., Nieh, T.G., Yamasaki, T., "Hall Petch Breakdown Manifested in Abrasive Wear Resistance of Nanocrystalline Nickel,"(2002) Scripta Mat. **47** pp. 735-740

[30] Kim, H.S., Estrin, Y., Bush, M.B., “Plastic Deformation Behavior of Fine Grained Materials,”(2000) Acta mat. **48,** pp.439-504

[31] Wang, Y.B., Li, B.Q., Sui, M.L., Mao, X.S., “Deformation induced grain rotation and growth in nanocrystalline Ni,”(2008) App. Physics Letters **92,** pp.011903-1-3

[32] Rosner, H., “HRTEM observation of interfacial dislocations to faceted Al-Pb interfaces,”(2004) Philosophical Magazine Letters **84**(321)

Chapter Two: Experimental Methods

2.1 Introduction

Mechanical properties testing of thin films is an area where "thinking outside the box" has led to the development of a variety of measurement techniques. From micromachined samples used to conduct tensile tests (Figure 2.1a)[1] to microbeam bending techniques (Figure 2.1b)[2], the measurement methodologies that scientists working on the nanoscale have come up with are becoming widely utilized.

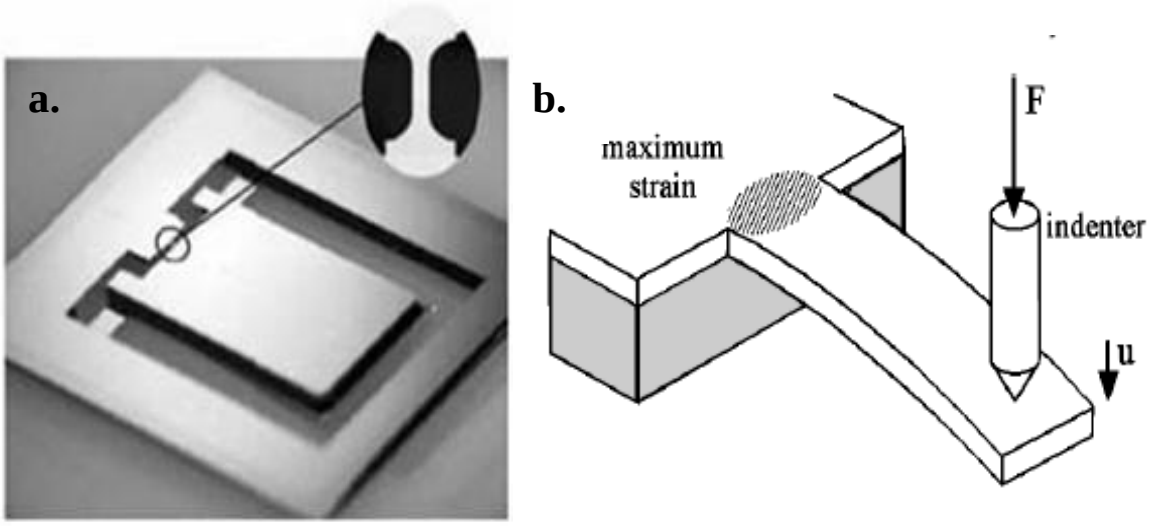

Figure 2.1 – Common micro-scale testing methods; a. shows a typical setup for micro-tensile testing[1] and b. shows the microbeam bending test.[2]

This chapter discusses a variety of experimental techniques including: photolithography, laser interferrometry, reactive ion etching, bulge testing, burst testing, nanoindentation and scanning electron microscopy.

Also discussed in this chapter is the development of a new pressure vessel for burst testing of the multilayer films, interesting effects of reactive ion etching, and fabrication copper films with high compressive stresses.

2.2 Making a Free Standing Film: Photolithography & Reactive Ion Etching

2.2.1 Photolithography – Window Fabrication

The first step when using photolithography is the development of a mask pattern. For this work, masks of the desired window geometries were made using CorelDraw. Before designing a mask, all subsequent processing steps should be clearly understood. For example, etching with EDP solution is highly anisotropic, leaving behind a (111) plane which makes an angle 54.7°[3] with the xy plane of the wafer. This is important, because, as seen in Figure 2.2, the dimensions of the final window for testing will be significantly smaller than the dimensions of the mask.

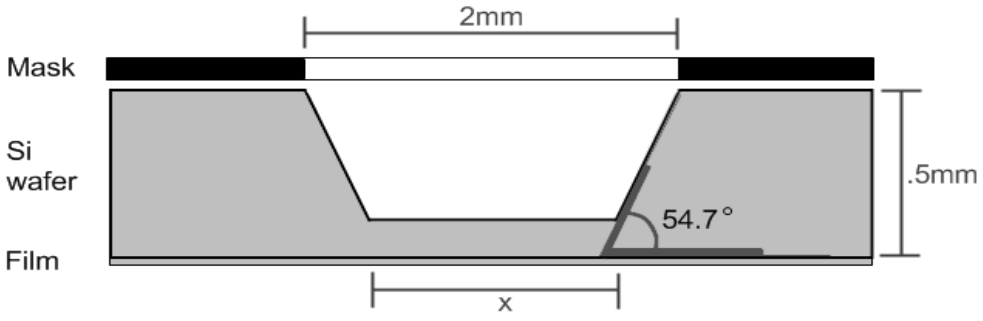

Figure 2.2– Schematic showing the decrease in window size due to anisotropic etch.

Photolithography used for the production of the window geometries in this study was limited to negative photoresists. Holes in the mask were exposed to UV light, then successively etched away to form windows A pictographic representation of this process

is included in Figure 2.3. The pattering and etching steps are described with the letter preceding each paragraph representative of the steps included in Figure 2.3

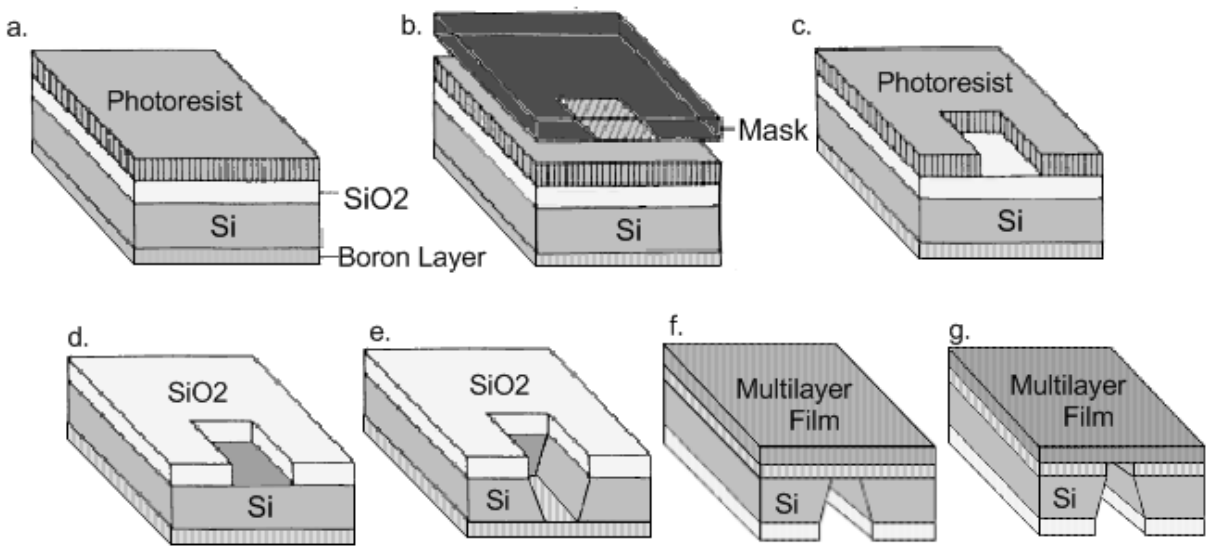

Figure 2.3 – Steps of Photlithography a)photoresist applied b)masked & pattered c)developed d)BOE etch e)EDP etch f)film deposition g)RIE etch

FIVE STEP CLEAN

Before beginning pattering, wafers were first cleaned with a five step cleaning process, sequentially using acetone, isopropyl alcohol (IPA) and de-ionized water to dissolve and remove any contaminants which may have ended up on the silicon wafer. After the water rinse, it is important to re-clean the surface with acetone and isopropyl alcohol a second time to remove any water left by the first rinse. Immediately following, the wafer was dried with nitrogen gas to prevent evaporation residue from depositing on the wafer. It should be noted that during this process care was taken to ensure that both sides of the wafer were cleaned, and at no point in the process was either side allowed to evaporate off.

PATTERNING & WET ETCHING

A) After cleaning, the wafer was spin-coated at 1500rpm with Hexamethyldisilane (HMDS) solution for 30 seconds. This process was then repeated, using the AZ5214 photoresist, then allowed to softbake on a hotplate at 110˚C for 60 seconds. After the wafer was allowed to cool, the process was then repeated on the back side of the wafer. It is very important that the HMDS and AZ5214 photoresist are applied to both sides of the wafer before continuing the process.

B,C) Patterning was accomplished using standard photolithography techniques with the aid of a Hybralign Series 500 PhotoMask Aligner. Once the desired pattern, made in CorelDraw, polymer masks were aligned with the silicon wafer and the film was exposed to UV light for 13 seconds. The photoresist was subsequently developed in a 4:1 solution of Deionized water:AZ400K developer solution for a total of 60 seconds.

D) Following developing, the wafers were rinsed with DI water and put into the buffered oxide etch (BOE) for nine minutes to remove the protective SiO_2 layer in the areas of the windows. Care was taken to thoroughly rinse off any excess BOE etchant while still in the BOE hood, after which the wafers were then taken through a second five step clean before continuing the process. Failure to coat both sides of the wafer with photoresist as seen in step “A” would result in removal of the etch stop (boron doped layer) and during step (E) the windows would become holes through the thickness of the wafer.

E) A second wet etch was then performed using a solution of ethylene diamine pyrocatechol (EDP) etchant. The EDP etch bath was heated to a temperature of 95˚C (which takes 4-5 hours) and the wafers were allowed to remain in the solution for 4.5 hours, checking their progress at 3.5 hours. The purpose of the boron doped layer is evident in this step, it acts as the etch stop, preventing the EDP etchant from continuing through the entire thickness of the wafer. This occurs because the highly anisotropic EDP etchant does not attack heavily p-doped silicon. It is very important when performing the EDP etch that the solution temperature during etching should remain between 95˚C and 100˚C. "At temperatures less than 95˚C insoluble residues develop, while at temperatures above 100˚C the etch rate increases rapidly to the point that tolerance control becomes difficult."[4] After removal from the etchant, an initial DI water rinse and a third five step clean is performed.

F) Multilayer films were then deposited using a sequential sputtering technique with a DC magnetron sputtering system at Los Alamos National Labs in the CINT facility operated by Dr. A. Misra. Deposition was performed at room temperature alternating between copper, nickel and niobium until a final thickness of approximately 2μm was reached. The elemental films of copper and gold fabricated at Washington State University also using an Edwards Auto 306 DC magnetron sputtering system.

Due to the very high tensile stresses seen in the CuNi multilayers and the poor adhesion of this film system, it is recommended for future testing the window structure seen in Figure 2.1e. be plasma etched in an oxygen environment before deposition of the

film. This would ideally alter the surface enough so as to promote better adhesion of these films, and prevent the spontaneous delamination of the CuNi films from occurring. Silicon Nitride support layers were also used for preliminary testing of CuNb films. A second possible alternative which could promote better adhesion of the CuNi layers would be to attempt deposition of these films onto SiN_x support layers.

2.2.2 Reactive Ion Etching

G) Reactive ion etching was used to remove the substrate backing for testing of the free standing films. Samples were etched with the use of a South Bay Technologies RIE 2000 equipped with an MKS mass flow controller. Processing parameters during etching were maintained at 100W and approximately 100 mTorr. An 18 minute etch time was used, in an atmosphere of 95% CF_4 and 5% O_2 to remove the boron doped substrate layer. Etch times were determined experimentally by performing the etch on film-less substrates (Figure 2.3e) until the substrate was completely removed. During batch etching of multiple samples, a film-less substrate was included to ensure complete removal of the substrate.

The process of reactive ion etching led to several interesting developments in the film structure. The first of which was an observable color change in the films after reactive ion etching. It would be ideal if the reactive ion etching process used to prepare free standing films caused no damage to the remaining metallic film. However, after exposure to the RIE environment a change in film color, from “silver” to a “copper” color as seen in Figure 2.4 was observed.

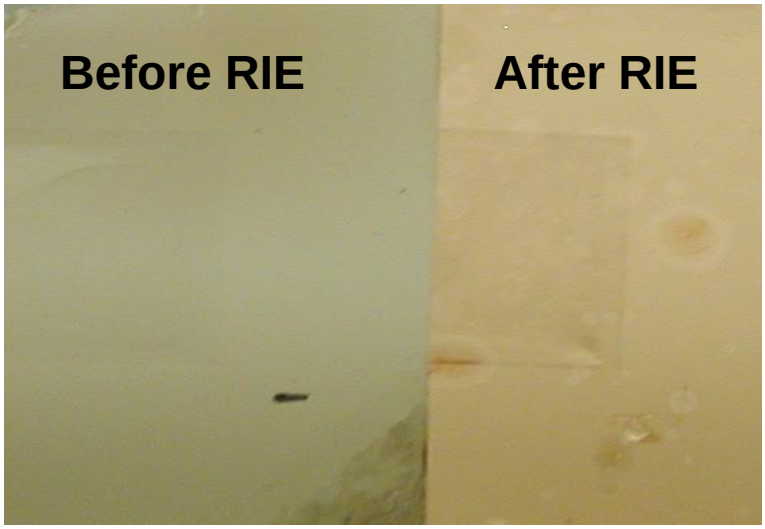

Figure 2.4 – Change in color of multilayer film observed after reactive ion etching step.

This suggests a slight amount of etching may occur on the freestanding film during RIE processing. However, by comparing the bulge test results of substrate backed films to reactive ion etched films, no significant difference was observed. The full analysis of this effect is discussed in more detail in chapter three.

A second effect made visible by reactive ion etching of single layer copper films was that of the film's stress state. Several 0.75μm copper films were sputter deposited in an effort to validate the results of the bulge test method and to compare results to those of the multilayer films. However, after reactive ion etching the sputtered Cu films it was evident that the high compressive stresses of these films would not allow for accurate properties determination via bulge testing. Figure 2.5 depicts a compressively stressed Cu film after reactive ion etching. Buckling is clearly visible in the freestanding film.

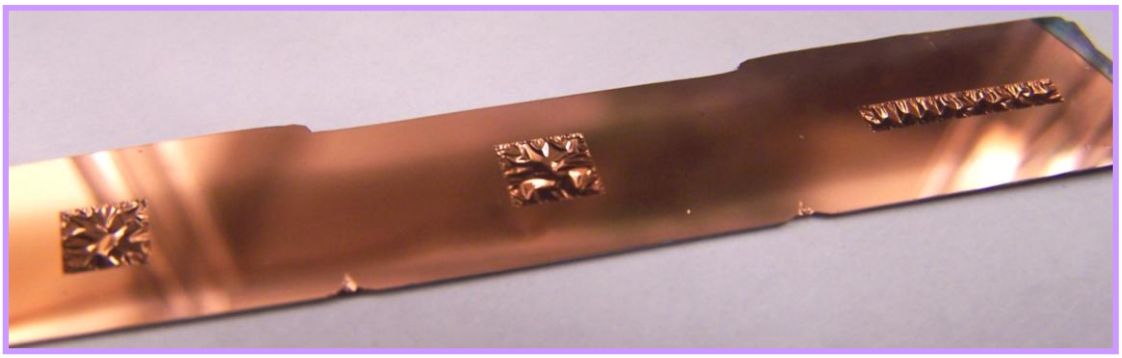

Figure 2.5 – Compressive stress induced buckling made visible after Si-SiO_2 substrate was removed by reactive ion etching.

In an effort to eliminate these effects, copper films were sputter deposited at a variety of pressures: 7mTorr, 4mTorr and 1.8mTorr in an effort to deposit a tensile stressed film, as outlined in Figure 2.6 [5] however, even with this variety of pressures the transition was never reached and therefore the compressive stress state was never completely eliminated.

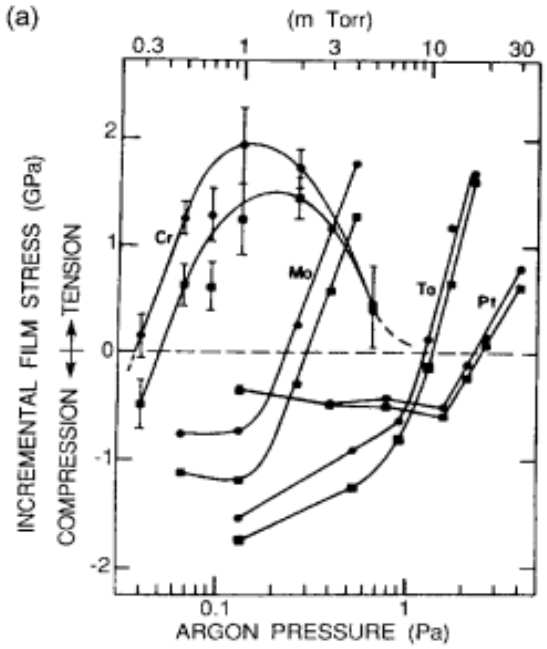

Figure 2.6 - Diagram of several metals showing the transition from tensile to compressive stresses as a function of pressure.[5]

Several attempts were made to relieve these stresses including annealing in an argon atmosphere 550˚C for one hour and also immersing in a 75˚C mineral oil bath for 25 minutes. While none of the attempts were successful, the mineral oil bath yielded the most promising results, eliminating nearly all buckling except at the perimeter of the windows. Annealing as shown in Figure 2.7 was shown to severely embrittle the film, and lead to widespread cracking. For these reasons, gold was chosen instead of copper to provide a validation of the bulge testing method.

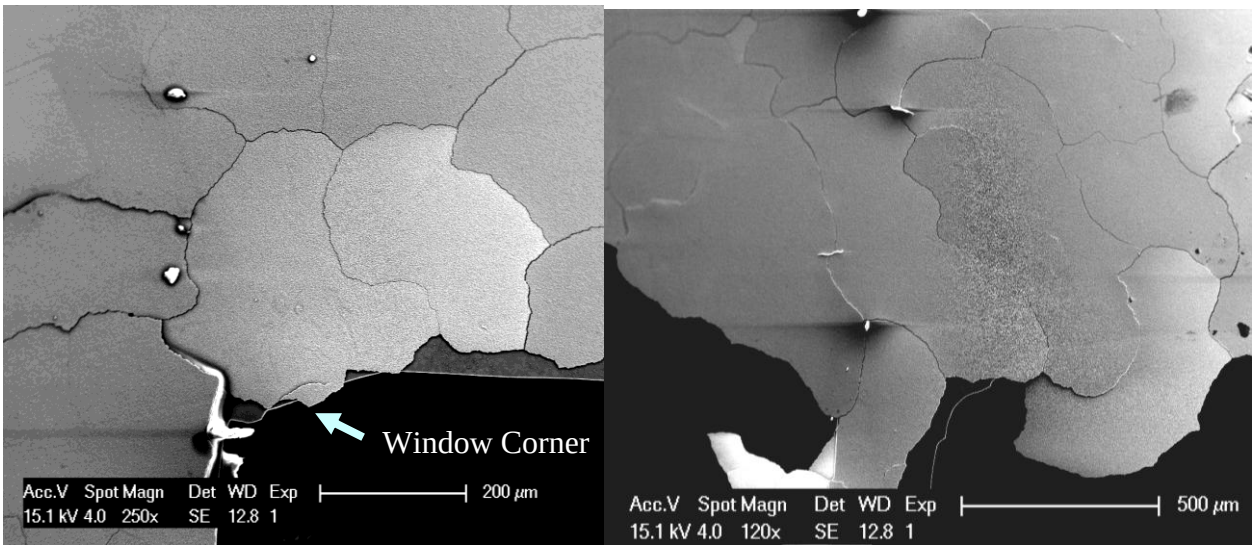

Figure 2.7 – SEM images of two different locations on embrittled film after annealing.

2.3 Laser Interferometry

2.3.1 Overview

Laser vibrometry uses the doppler effect to measure vibration.[6] If light is scattered from a moving object its frequency is changed slightly. "Within a polytec vibrometer, a high precision interferometer detects the minute frequency shifts of the backscattered laser light."[7] To achieve this, the interferometer splits the light into two parts, a reference

beam and a measurement beam. The reference beam is pointed directly to the photo-detector while the measurement beam is focused on the test specimen. Figure 2.8 shows a schematic diagram of this.

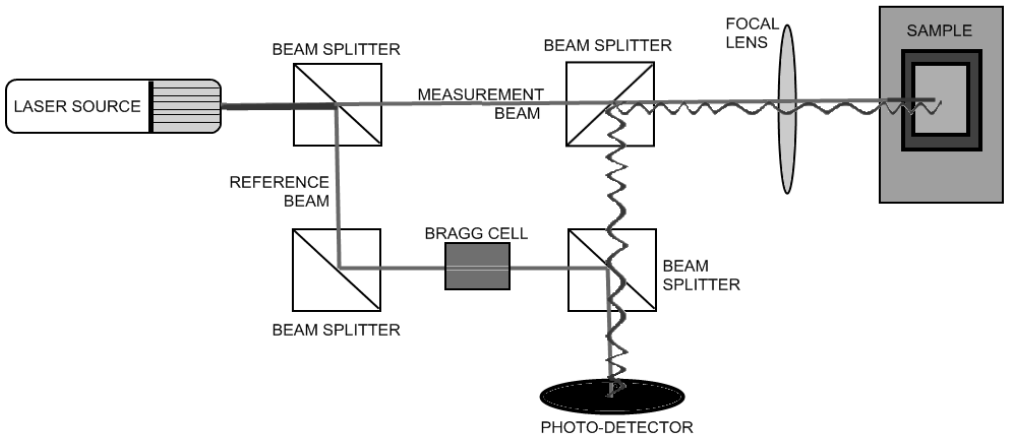

Figure 2.8 – Schematic of laser vibrometer showing reference and measurement beams.

During a test, light is scattered as the membrane goes through its pressure/deflection cycles. Depending on the amount and rate of membrane movement, the velocity and displacement of the laser beam are altered in frequency and phase.[8] The superposition of this altered light beam with the reference beam creates a modulated detector output signal revealing the doppler shift in frequency via the Bragg cell [7] and the difference in path length. Subsequent signal processing and analysis provides the vibrational velocity and displacement of the test object.

2.3.2 Displacement Calculation

In this study, only the displacement of the thin film membranes was measured. As the photodetector measures the intensity of the two beams, this intensity (I) is related to the the phase difference ($\Delta\varphi$) by

$$I(\Delta\varphi) = \frac{I_{max}}{2}(1+\cos(\Delta\varphi)) \qquad (2.1)^{9}$$

where the phase difference is a function of the path difference (L) between the two beams and the wavelength λ of the laser light, which can be written as:

$$\varphi = 2\pi\left(\frac{L}{\lambda}\right) \qquad (2.2)^{9}$$

Because the laser interferometer used in this study is a helium-neon laser, (visible & red) the wavelength of the light is 632nm. The resolution of the laser used in the bulge tests set-up is in the sub-nanometer range.[9]

2.3.3. Operating the Laser Vibrometer

When using the laser vibrometer, there are several important measurement aspects to consider. First is that the laser is centered directly over the portion of the sample where deflection measurements are desired, and vertically aligned (Figure 2.9).

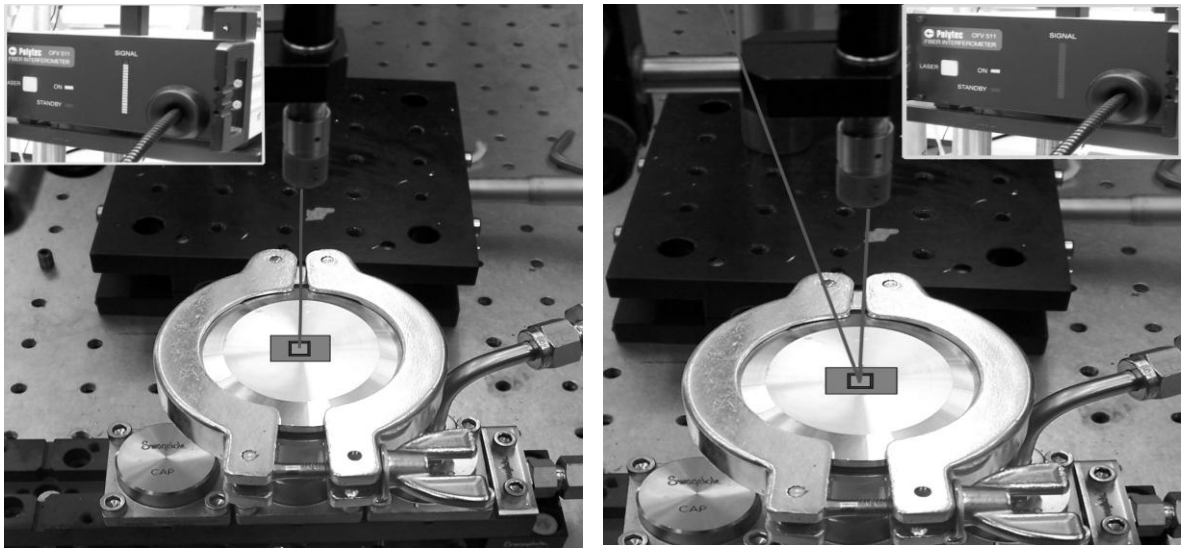

Figure 2.9 – Showing alignment of laser and good signal (left) and poor alignment (right).

Secondly, it is important to ensure that the "signal" and "trigger" cables leading from the amplifier are plugged into the vibrometer controller.(Figure 2.10)

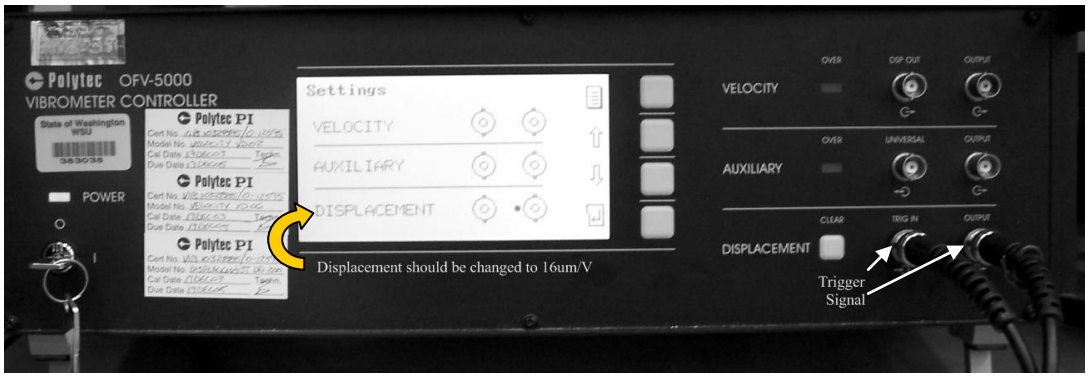

Figure 2.10 –Vibrometer controller box showing cables inserted and displacement setting.

After turning on the vibrometer controller, the displacement setting should be selected and the range changed to 16µm/volt. The range can be modified, but in order to do so correctly, this modification should be made to the LabView program in addition to the vibrometer controller. And lastly, for future vibrometer users who refer to this work, please do not bend or kink the laser cable as this part contains fiber optics.

2.4 Bulge Testing Method

Bulge testing was performed on a wide variety of sample geometries for this study. A discussion of each is included with the respective equations that were used to determine film properties.

2.4.1 Performing a Test

Operation of the bulge test apparatus is fairly straightforward. The aluminum mounting pucks are heated on a hotplate at a setting of 6 for approximately 45 seconds. Membrane samples are mounted on the aluminum puck using Crystal Bond 555 wax. The wax will then melt when it reaches a temperature of 29ºC (as measured with a Rytech Laser thermometer) at this time, the film/substrate can be mounted . Extra care should be taken when mounting so that minimal amounts of wax are melted onto the surface of the hot puck, this is because excess wax will wick up into the membrane and adhere to the film. Though not visible when in the liquid state, if large amounts of wax are allowed inside the membrane cavity, as the wax dries it will expand, deforming the membrane and leading to inaccurate measurements.

After mounting the sample, the laser vibrometer is turned on and aligned with the center of the membrane until the signal is at 90-100% full scale. The settings for the vibrometer can be found in the previous section. Warm-up time for the vibrometer is on the order of 45-60 minutes. The labview program entitled “Bulge Test Program” can then be opened. With the bellows valve open so atmospheric pressure can be recorded the “run” option can be selected. By watching the instantaneous defection vs. time plot after about 30 seconds the laser will stabilize. “STOP” can then be activated, this records the atmosphereic pressure and stops the deflection measurements. The bellows valve should

then be closed, and the "Zero and Start Experiment" button can be selected. This re-zeros the last deflection measurement and records real time pressure deflection data. By turning the bellows crank, both positive and negative (vacuum) pressure can be applied.

2.4.2 Elastic Property Determination

The pressure deflection relationship[10-13] obtained during a bulge test is of the form:

$$P = Ah + Bh^3 \tag{2.3}$$

where the pressure *(P)* is a function of the deflection (*h*). After the raw test data is generated, is it then curve fit to an equation of this form which yields numerical values for constants *A* and *B*. As shown in Figure 2.11 the results of bulge testing for this study clearly fits the generic membrane equation.

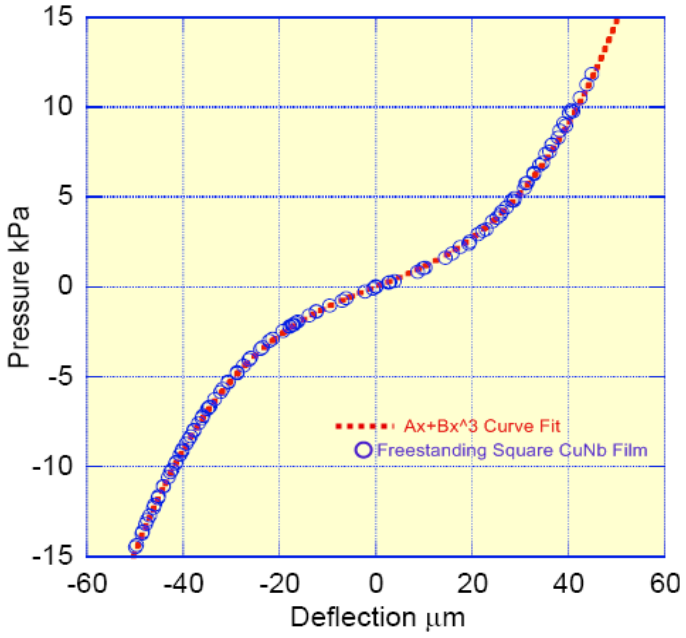

Figure 2.11 – Raw pressure deflection data (blue) compared to a curve fit using the generic membrane model.

The generic model can also be modified to account for any initial offset errors that could occur due to poor signal or vibrations at the start of the experiment. While of the same form as Equation (2.3), Equation (2.4) below incorporates an initial deflection offset, h_o and an initial pressure offset, P_o.[14]

$$P = A(h - h_o) + B(h - h_o)^3 + P_o \tag{2.4}$$

The residual stress is determined from the linear coefficient and the elastic modulus from the cubic term. The full equations for each geometry are as follows.[14-17]

$$P_{circular} = \frac{C_1 \sigma_o t}{a^2} h + \frac{C_2 E t}{a^4 (1-\upsilon)} h^3 = \frac{4\sigma_o t}{a^2} h + \frac{8Et}{3a^4 (1-\upsilon)} h^3 \tag{2.5}$$

$$P_{square} = \frac{C_1 \sigma_o t}{a^2} h + \frac{C_2 E t}{a^4 (1-\upsilon)} h^3 = \frac{3.4\sigma_o t}{a^2} h + \frac{1.83 E t}{a^4 (1-\upsilon)} h^3 \tag{2.6}$$

$$P_{rectangular} = \frac{C_1 \sigma_o t}{a^2} h + \frac{C_2 E t}{a^4 (1-\upsilon^2)} h^3 = \frac{2\sigma_o t}{a^2} h + \frac{4Et}{3a^4 (1-\upsilon^2)} h^3 \tag{2.7}$$

For any given geometry listed, by using the curve fit value for *A* and setting this equal to the terms preceding "*h*" in Equations 2.5-2.7, with thickness(*t*), half the side length(*a*), poisson's ratio(υ) and the geometric coefficient C_1 known, the residual stress (σ_o) can then be calculated. In the same manner, the elastic modulus is determined using the curve fit value for *B* and solving for *E*. For the data in this thesis, the thickness of the films were measured by scanning electron microscopy, Poisson's ratio was assumed to be

0.25 for all samples. Images of the windows were taken and ImageJ was used to extract the side length.

It is very important to consider the stress state of the film when extracting properties and bulge testing different sample geometries. For example, in the case of square films which are in a state of biaxial tension, the *B* coefficient will yield a biaxial modulus (*M*) which must be converted to Young's modulus (*E*) using,

$$M = \frac{E}{1-\upsilon} \tag{2.8}$$

Where υ is Poisson's ratio. In the full equations listed this effect has already been taken into account. However, a thorough understanding of these equations is necessary, in order to correctly interpret the results of bulge test experiments performed by other researchers so that errors do not propagate. For example, for the complete derivation of the rectangular equation, the reader is referred to appendix I of [17]. While the derivation and final solution of this equation is mathematically sound, it is important to be aware of published work[18] referring to [17] where the final solution has been recorded incorrectly .

Analysis of the data gathered showed a fairly normal distribution in elastic modulus values, which is compared to results from nanoindentation in section 2.6.

2.4.3 Plastic Properties Determination

CIRCULAR GEOMETRY

To determine the stress and strain in a circular membrane, the widely used spherical cap approximation was used. In this approximation the bulge is modeled as a

biaxially stressed membrane which takes the shape of a perfect hemisphere of radius (*r*) as it is bulged, Figure 2.12.

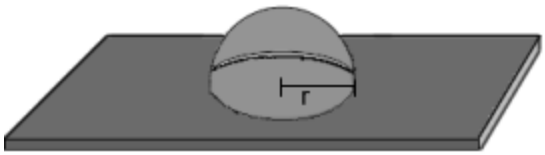

Figure 2.12 – Diagram of a spherical cap membrane geometry of radius r.

The strain in this film (ε) can then be expressed as the sum of the residual strain in the initially flat film and the strain due to the membranes deflection (*h*).

$$\varepsilon_{Total,xx} = \varepsilon_o + \frac{2h^2}{3a^2} \tag{2.9}$$

The stress at the center of the spherical membrane is then calculated using Hooke's Law to relate the stress and strain. Because a state of equibiaxial strain ($\varepsilon_{xx} = \varepsilon_{yy}$) is encountered at the centers of circular and square membranes, the equation for stress shown by :

$$\sigma = \frac{E\varepsilon_{Total}}{1-\upsilon} or \frac{Pa^2}{4ht} \tag{2.10}$$

where σ is the stress at the center of the membrane, and (*a*) is the radius of the membrane. For this work, the latter equation for stress was used.[10,19] Since the calculations to find the stress and strain in these membranes are based on isotropic linear elasticity theory, past the yield point these equations become invalid as is also the case with those of the square membranes.

SQUARE GEOMETRY

In a circular membrane, because it is axially symmetric no shear stress or strains are present.[14] The square geometry films are different in the fact that they only have two planes of symmetry. Because of this, maximum shear stress does not exist at the same point where the principal stresses are, except on the planes of symmetry (through the midpoints of the edges) and at the intersection of these planes (the center of the membrane.)[14] For this reason, the maxiumum Von Mises stresses occur at the centers of the edges and these stresses drop to zero at the corners of the membranes where shear stresses dominate. For this geometry, analysis of plastic deformation becomes difficult because the deformation is non-uniform. Some areas of the window deform plastically while others are still in the elastic regime. Finite element analysis of the square membrane was performed using ABAQUS and is discussed in detail in Chapter 3.

The stress distribution in square windows was studied by Hoelfelder[14] who modeled the stress distributions of this window geometry in detail. Using the results of these models, the stress and strain at the center of the membrane are calculated as:

$$\sigma_{square} = f(v) \cdot \frac{E \cdot h^2}{a^2} \tag{2.11}$$

$$\varepsilon_{square} = \varepsilon_o + f(v) \cdot \left(\frac{Pa}{Et} \right)^{2/3} \tag{2.12}$$

where $f(\upsilon)_{stress}$=.423 and $f(\upsilon)_{strain}$=.313 for υ=.25 And as was the case for the circular membrane, Equations 2.11 and 2.12 are linear elastic in nature and do should not be used to interpret data past the yield point.

RECTANGULAR GEOMETRY

The rectangular geometry is the last of the tested geometries for this study and arguably the most useful. A pressurized rectangular membrane that has an aspect ratio of at least four, is considered infinitely long. This is significant because the membrane is then only bound by its shortest dimension (2a). Because thin films show no through the thickness deformation, the rectangular geometry is in a state of plane strain making it particularly useful for analysis of plastic flow. For the rectangular geometry, the stress and strain relationships are:

$$\sigma_{\text{PlaneStrain}} = \frac{a^2 P}{2Ht} \qquad (2.13)$$

$$\varepsilon_{planestrain} = \varepsilon_o + \frac{2h^2}{3a^2} \qquad (2.14)$$

2.5 Burst Testing – Pressure Vessel Design

To achieve the higher pressures necessary to rupture the freestanding multilayer membranes, several modifications were made to the existing bulge test set-up including

calibration and implementation of a new pressure sensor (Figure 2.13), and the development of a new test vessel (Figure 2.14).

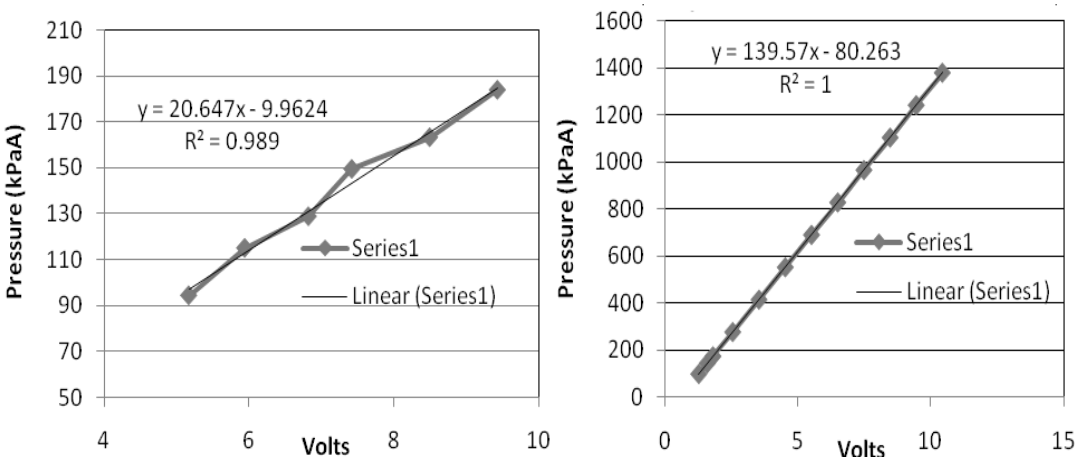

Figure 2.13 – Pressure sensor calibration curves for low pressure analysis up to 95kPa for the 30 psiA pressure sensor (left) and high pressure analysis to 900kPa+ using the 200psiA pressure sensor (right)

Instead of the clamp used in 2.14, a new chamber with threaded cap was specifically designed to operate at the higher pressures available when the system is plumbed with a nitrogen tank.

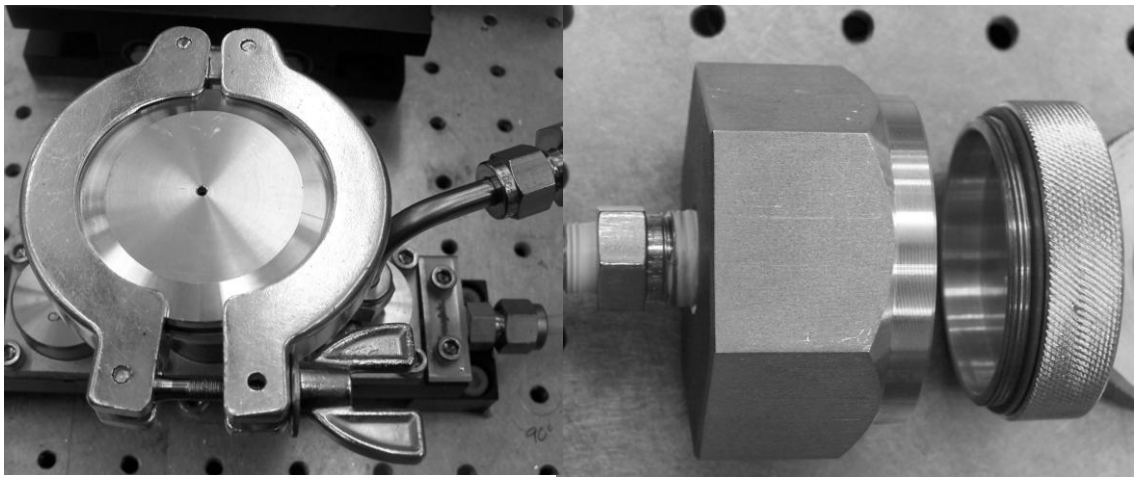

Figure 2.14 – Low pressure bulge test Chamber (left) high pressure test chamber (right).

Using this set-up the sample is mounted (film side up) on the inside of the cap and the laser measures deflection through a machined slot on the cap. As the cap is threaded onto the base, it tightens down onto an o-ring. When mounting samples using this pressure vessel, the o-ring should be removed as the cap is heated on the hotplate. Failure to do so will cause the o-ring to crack and pressure will not be maintained during testing. A cross-sectional view of the high pressure test chamber is shown in Figure 2.15.

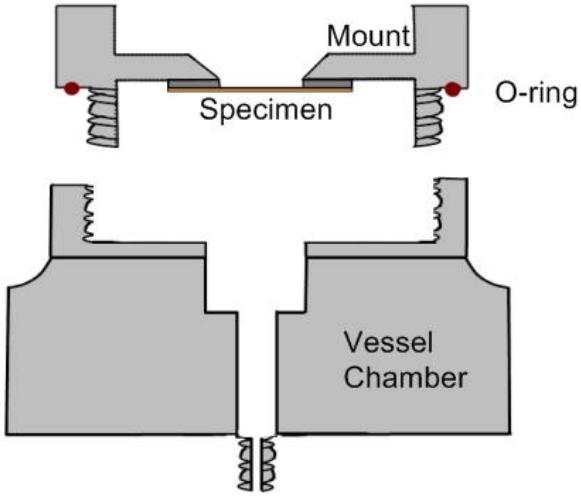

Figure 2.15 – Cross sectional view of high pressure vessel showing mounting orientation.

Without the development of this test vessel, failure of the multilayer films would not have been possible. The previous testing set-up was limited to approximately 400kPa, wherein pressure leaks would begin to occur along the clamp surface. With this new vessel, pressures of 950kPa were reached; this is not the maximum possible pressure, but was the maximum tested in this thesis.

2.6 Nanoindentation

Nanoindentation used in this thesis was performed in both the quasi-static and dynamic modes with the use of a Hysitron Triboscope nanoindentation system with nanoDMA attachment. Berkovich indenter tips were calibrated in Fused quartz before use. DMA measurements were performed using an AC oscillation of 30Hz. A brief discussion of nanoindentation methodology is outlined further.

The Oliver and Pharr method was used for determining the modulus and hardness values. During a measurement, the indenter tip is driven into the sample material and a specific load is applied. As the load is removed, the reduced modulus is then calculated from the unloading curve. This method is based on the empirical observation that unloading curves follow a power law relation which makes determining the initial unloading slope a simple mathematical construct after curve fitting the unloading data to a power law form[20]. The reduced modulus E_r can then be calculated by taking into account the measured compliance C, frame compliance C_f and the contact area of the indentation, A. The compliance of the load frame shown is then:

$$C = C_f + \frac{\sqrt{\pi}}{2E_r} * \frac{1}{\sqrt{A}} \tag{2.15}$$

Calculation of the Young's Modulus from the reduced modulus can be done using,

$$\frac{1}{E_r} = \frac{1-\upsilon_i^{\,2}}{E_i} + \frac{1-\upsilon_s^{\,2}}{E_s} \tag{2.16}$$

where E_r is the reduced modulus and υ is Poisson's ratio. The respective subscripts reference properties of the indenter tip E_i and υ_i or properties of the sample E_s and υ_s. [21]

Young's modulus of the Berkovich indenter tip is taken as 1249 GPa with Poisson's ratio equal to 0.07. [22]Calculation of the indentation area, *A* for this thesis was experimentally calibrated in quartz over the depth range (0-160nm) which would minimize substrate effects.

Results from Bulge test data were compared to those of nanoindentation. Both methods showed fairly normal distributions as seen in Figure 2.16 and agreed with each other to within 10%. Average values and standard deviations for these measurements can be found in Champer 3 of this thesis.

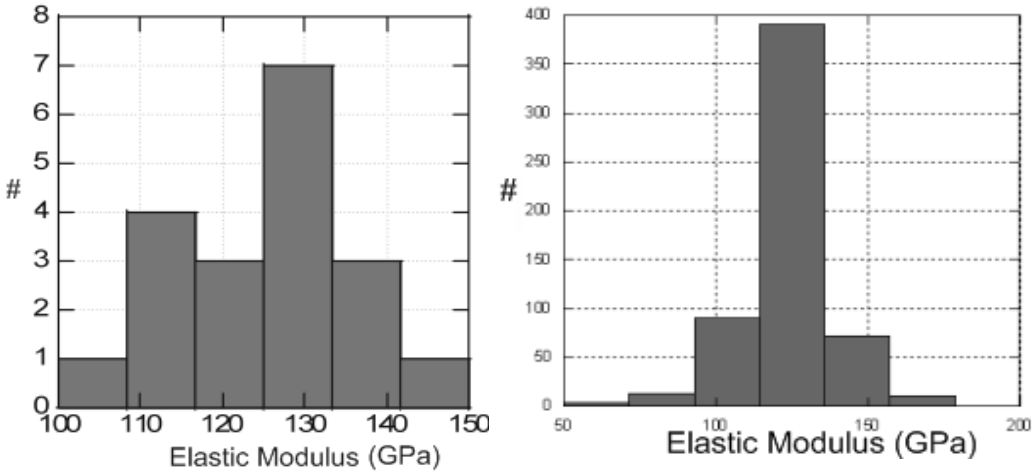

Figure 2.16 – Histograms of CuNb thin films measured by bulge testing (left) and nanoindentation (right).

2.7 Microscopy

The dominant mode of microscopy used in this thesis was scanning electron microscopy. The field emission SEM was used for a variety of purposes including: grain size measurement, film thickness measurement and overall featural analysis of the

multilayered films. Operation of the SEM was typically performed between 10keV-25keV. Mounting samples onto silver paint, as opposed to conductive tape, improved imaging of the films (while still mounted on the substrate) dramatically.

2.8 References

[1] Sato, K., "Three dimensional fine structures created by etching –Micro/nano processing using crystal anisotropy,"(2006) Japan Nanonet Bulletin (90) Online accessed www.nanonet.go

[2] Kraft, O., Volkert, C.A., (2001), "Mechanical testing of thin films and small structures," Advanced Engineering Materials, **3**(3) pp.99-110

[3] Vazsonyi, E., Vertesy, Z., Toth, A., Szlufcik, J., "Anisotropic etching of silicon in a two component alkaline solution," J. Mecormech.Microeng. **13** pp.165-169.

[4] Reisman, A., Berkenblit. M., Chan, A.S., Kaufman, F.B., Green, D.C., "The Controlled Etching of Silion in Catalyzed Ethylenediamine Pyrotechol Water Solutions," (1979) J. Electrochem. Soc., **126**(8) pp. 1406-1415

[5] Ohring, M., "Materials Science of Thin Films" Academic Press, 2002.

[6] Hecht, E., "Optics – Second Edition" Addison Wesley, 1987.

[7] Martin, P., Rothberg, S., "Introducing speckle noise maps for Laser Vibrometry," (2009) Optics and Lasers in Engineering 47 431– 442

[8] Author Unknown "Vibrometry Basics" (2007) Online accessed: www.polytech.com

[9] Author Unknown, "Polytec User Manual - Polytech User Manual Fiber-optic Vibrometer Sensor Head OFV-511-512" Waldbronn, Germany, 2003.

[10] Sauter, W. "Thin Film Mechanics Bulging and Stretching," (2002) PhD Thesis, University of Vermont, USA.

[11] Small, M.K., Nix, W.D., "Analysis of the accuracy of the bulge test in determining the mechanical properties of thin films," (1992) J. Mater. Res. **7**(6) pp.1553-1563

[12] Lee, H.k., Ko, S.H., Han, J.S., Park, H.C., "Mechanical Properties Measurement of Silicon Nitride thin films using the bulge test," (2007) Microelectronics **6798**(1C), pp.67981C.1 – 67981C1.8

[13] Xiang, Y., Chen, X., Vlassak, J.J., "Plane strain bulge test for thin films." (2005) J. Mater. Res. **20**(9), pp.2360-2370

[14] Hohlfelder, R.J., "Bulge and Blister Testing of Thin Films and Their Interfaces," Ph.D., Stanford University, 1999.

[15] Kalkman, A.j., Verbrugger, A.H., Janssen, G.C.A.M., Groen, F.H., "A novel bulge-testing setup for rectangular free standing thin films." (1999) American Institute of Physics **70** (10) pp.4026-4031

[16] Small, M.K., Daniels, B.J., Clemens, B.M., Nix,W.D., "The elastic biaxial modulus of Ag=Pd multilayered thin films measured using the bulge test," (1994) J.Mater.Res. **9**(1) pp. 25-30.

[17] Vlassak, J.J., Nix., W.D., "A new bulge test technique for the determination fo Young's modulus and Poisson's ratio of thin films," (1992) Mat. Res.Soc., **7**(12) pp.3242-3249

[18] Mitchell, J.S., Zorman, C.A., Kicher, T., Roy, S., Mehregany, M., "Examination of Bulge Test for Determining Residual Stress, Youngs Modulus, and Poisson's Ratio of 3C-SiC Thin Films," (2003) J.Aerospace Eng., **16**(2), pp.46-54

[19] Jankoski, A.F., Tsakalakos, T., "Effects of deflection on bulge test measurements of enhanced modulus in multilayered films." (1996) Thin Solid Films, **290,** pp.243-247

[20] Nibur, K. A. "Nanoindentation Slip Steps and Hydrogen Embrittlement" (2005) Ph.D., Washington State University pp1-131

[21]Hoehn, J.W., "Micromechanical Probes of Anisotropic Nitrides and Aluminides," "Theory & Background of Nanoindentation & Microscratch Tests" Ph.D., Washington State University pp. 31-59

[22] Chen, S., Liu L., "Investigation of the mechanical properties of thin films by nanoindentation, considering the effects of thickness and difference coating-substrate combinations." (2005) Surface and Coatings Technology. **191**(1) pp. 25-32

Chapter Three:

Yield and Deformation in Biaxially Stressed Multilayer Thin Films

**The majority of information contained in this chapter has been reviewed and accepted for publication in the Journal of Engineering Materials Technology.*

3.1 Introduction

Nanoscale engineered materials are an area of emphasis in materials research because of their enhanced mechanical properties compared to bulk materials as discussed in Chapter 1. Nanolaminate thin film materials in particular are of significant interest due to their ultrahigh strengths and hardness [1-3] as well as their potential resistance to radiation damage[4]. While the most common method of assessing the mechanical properties of thin films is nanoindentation, there are also examples of tensile tests performed at these length scales. These tests can be either MEMS fabricated tensile tests[5] or free standing bulk tensile tests.[6] However, there are limitations in both the size of the testing structure and in the processing of the samples which makes bulge testing a particularly attractive testing methodology. The advantages of bulge testing are its ability to test freestanding films in a variety of geometries, and the ease in which samples fabricated in this manner can be coupled with alternate testing methods [7-14].

The enhanced mechanical response of bilayer metallic composites over their constitutive components is well documented. When individual layers are on the order of 100 nm or greater in thickness, these films tend to follow a Hall-Petch type behavior where the film thickness replaces the grain size as barriers to dislocation transmission.

When film thicknesses are substantially less than 100 nm, a variety of mechanisms have been proposed to explain the decreasing effectiveness of grain size dependence. The modified confined layer slip model (CLS)[15] has been used to describe the properties in this thickness range, and has been shown to accurately capture the effects of layer thickness on the flow stress in multilayer metallic composites. As multilayer films are strained to fracture in tension there is direct evidence that the plastic zone is highly confined to the region in the vicinity of the crack tip[16], and that there is the likelihood that crack tip blunting may occur in Cu/Ni multilayers. Therefore, examining the early stages of plastic deformation as well as higher strain conditions is needed for understanding failure mechanisms in metallic multilayer composites, particularly for developing fatigue testing schedules.

The CLS phenomena has been observed in both FCC-FCC and FCC-BCC materials, the FCC-FCC systems will have additional coherency stresses that may impact plasticity[15]. In addition, while in plane orientations are random, previous studies on these film systems have shown a strong Kurdjumov-Sachs orientation relationship out of plane with: {111}Cu ‖ {110} Nb and <110> Cu‖<111> Nb [2,15]; while CuNi films have been shown to exhibit a cube on cube orientation relationship.[1] The current study examines the elastic and plastic properties of Cu-Nb, Cu-Ni and Cu-Nb-Ni multilayer thin films using bulge testing in conjunction with nanoindentation. Identification of the microscale yielding behavior of these material systems in addition to the strain hardening behavior will allow for a better understanding of appropriate operating pressures for fatigue testing in the future.

3.2 Procedures

Films were deposited onto silicon substrates that had been both boron doped and oxidized, with a boron doped layer approximately 2 μm thick and a thermally grown oxide with a thickness on the order of 150 nm. Standard photolithography techniques were utilized to create different window geometries. Samples were micromachined in a wet anisotropic etch to form membranes with nominal lateral dimensions of 4mm x 4mm and 1.5mm x 10mm for the square and rectangular specimens respectively. The films were deposited onto the Si/SiO_2 windows at room temperature using a dc magnetron sputtering system. Multilayer fabrication consisted of alternating 20nm layers of Cu, Nb, and Ni until a final thickness of approximately 2μm was reached. Reactive Ion etching was used to remove the substrate backing resulting in a free standing film for testing. Samples were reactive ion etched with a South Bay Technologies RIE 2000 equipped with a mass flow controller. An 18 minute etch time was used, in an atmosphere of 95% CF_4 and 5% O_2 to remove the Si/SiO_2 substrate layer. Processing parameters during etching were maintained at 100W and approximately 100 mTorr.

During bulge testing, the displacement at the center of the membrane was measured using a Polytec OFV 511 scanning laser vibrometer. Pressure was applied to the membrane using a Meriam Pressure/Vacuum variator. Because of the high yield strength, but low adhesion strength of these films, mounting orientations were chosen to eliminate the problem of film delamination during testing. Figure 1 shows the different loading configurations that were used.

Young's modulus values measured from bulge testing were confirmed using nanoindentation. Measurements of the mechanical response of the films were made using a Hysitron Triboscope nanoindentation system with nanoDMA attachment and Berkovich indenter tip. The sample was positioned using a Park Scientific Autoprobe CP Scanning Probe Microscope. Measurements were performed using an AC oscillation of 30Hz.

Non-linear elastic modeling of the square and rectangular membrane geometries was performed using ABAQUS. The geometries used were 4mm x 4mm for the square and 1.5mm x 10mm for the rectangle, both with a thickness 5μm. Analysis was performed using SR85 elements (reduced integration, eight node, doubly curved thin shell elements with five degrees of freedom per node.) The boundary conditions include fixed edges with zero degrees of freedom. Uniform loading was applied to the top surface and a stiffness of 120GPa was used to approximate the stiffness of the films tested.

3.3 Results and Discussion

3 .3.1 Elastic Properties of Free Standing Films

Bulge testing to determine elastic and plastic properties in multilayer metallic films allows for both biaxial and uniaxial testing depending on the membrane geometry. During a bulge test, film deflection is measured as a function of the applied pressure. As seen in Figure 1 the experimental setup used in these tests allows for testing in both a "positive" or "negative" direction shown in Figure 3.1.

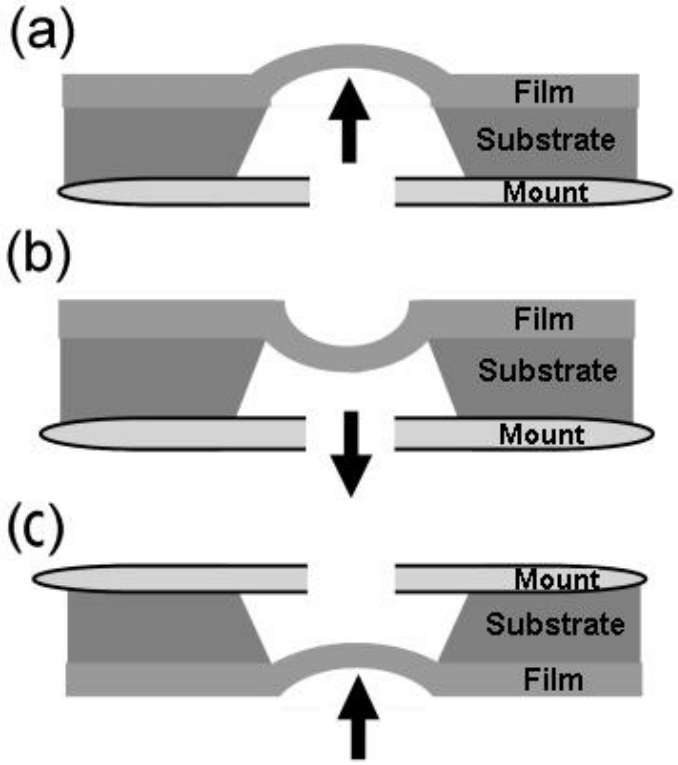

Figure 3.1- Schematic illustrations of mounting used A) mounting configuration leading to delamination of film. B) "Negative Pressure" orientation using vacuum C)"Positive Pressure" Orientation. All orientations depict a freestanding film after removal of the SiO_2 support window by reactive ion etching.

This significantly simplifies determination of the zero deflection condition for subsequent analysis of the membrane pressure – deflection relationship. At pressures where deformation is limited to the elastic regime the data is quite reproducible for any given membrane, as shown in Figure 3.2.

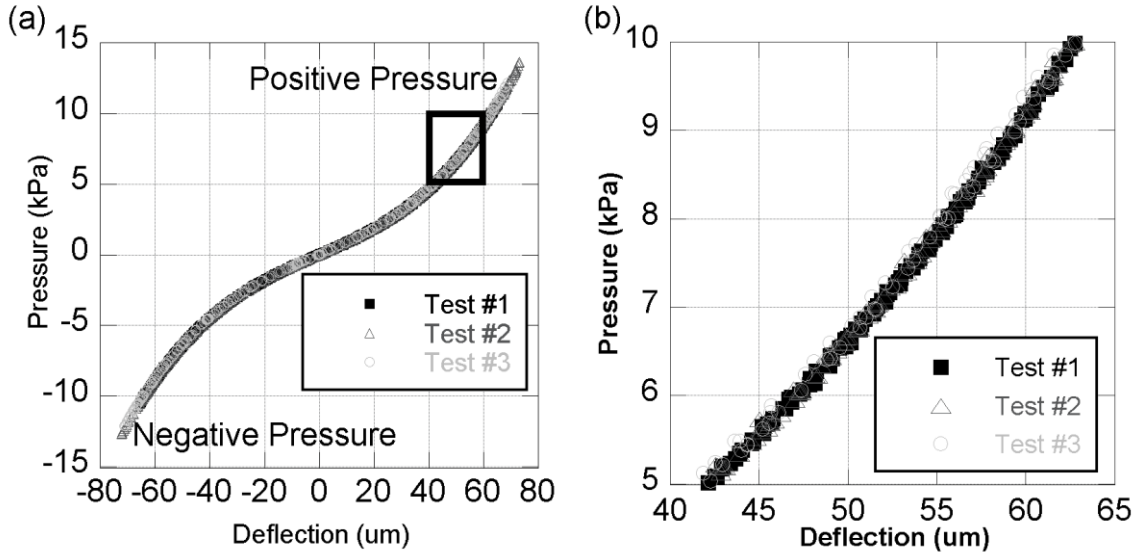

Figure 3.2- (a) Typical pressure deflection curves showing elastic deformation in a free standing CuNb square film. (b) An enhanced view of the highlighted region in (a) between 5 and 10kPa. Tests 1-3 show minimal deviation is seen after repeated testing of the sample.

The free-standing bulge test data can be fit to

$$P = \frac{C_1 \sigma_o t}{a^2} w + \frac{C_2 E t}{a^4} w^3 \tag{3.1}$$

where P is the pressure, a is one half of the side length, which for rectangular samples corresponds to the short side if an aspect ratio of at least 4 is maintained, t the film thickness, E is the Young's modulus, w is the center deflection, σ_r is the residual stress, and C_1 and C_2 are constants dependent on Poisson's ratio and membrane geometry which are listed in Table 1.[10,12,14,17,18] It is important to note that the calculation of the coefficient C_2 incorporates different functions of Poisson's ratio which account for E being defined as the Young's modulus for both square and rectangular geometries instead of a biaxial or plane strain modulus respectively. The residual stress σ_r can be extracted from the linear coefficient while the modulus is incorporated into the cubic coefficient.

Poisson's ratio was assumed to be 0.25 for all samples for uniformity. In calculating these properties, it should be noted that the conditions for which Equation 1 holds are that C_1 does not change for large deflections and that C_2 is not a function of σ_o.[8]

Table 3.1 Constants used for determination of materials properties from freestanding bulge tests.

Membrane Geometry	C_1	C_2	C_2 *including conversion to Young's Modulus for v=.25*
Square	3.39	1.83	2.44
Rectangle	2.0	$8/[6(1-v^2)]$	1.422

Bulge testing was performed on 21 CuNb samples, 7 CuNi samples and 5 CuNbNi samples. Results from CuNb multilayers for both square and rectangular geometries have an elastic modulus of 122.6±13.6 GPa which correlates well to the values for CuNb multilayer films presented by Misra and Wang.[2,14] CuNi specimens have an elastic modulus of 128.75± 9.47 GPa and the trilayer samples result in a modulus of 126.5±12.6 GPa. Residual stresses measured for these films ranged from 80-200MPa, with the CuNi specimens having the highest residual stresses.

3.3.2 Elastic Deformation of Substrate Backed Films

It would be ideal if the reactive ion etching process used to prepare free standing films caused no damage to the remaining metallic film. However, after exposure to the RIE environment a slight optical color change (from "silver" to a "copper" color) was observed. This suggests a slight amount of etching may occur on the freestanding film during RIE processing. To ensure this damage was negligible, bulge tests were carried out on the CuNb multilayers while still attached to the substrate and compared to those of

the RIE processed free standing films. To carry out these tests, samples were mounted and bulge tested. Then, due to the relatively weak adhesion strength in these samples the films were mechanically removed from the substrate over the region of the window, leaving the Si/SiO_2 window behind. Bulge testing was then repeated on the Si/SiO_2 windows alone. The pressure-deflection relationship between the substrate window and substrate with film is shown in figure 3.3.

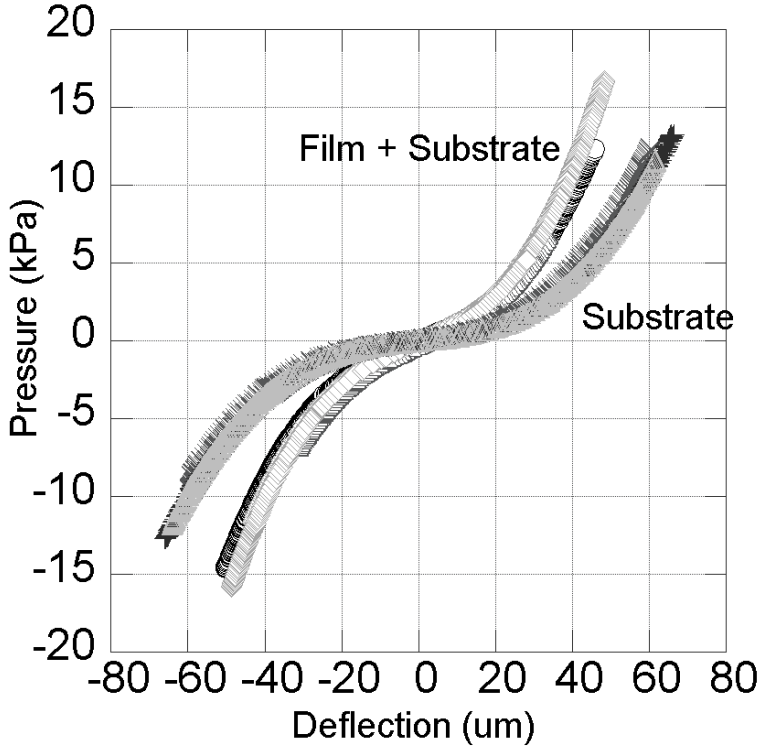

Figure 3.3- Pressure-deflection curves showing substrate / film + substrate

A simple rule of mixtures was then used to normalize the effective composite biaxial modulus and extract the biaxial modulus of the film, M_f[13]

$$M_{COMPOSITE} = \frac{t_F}{t_T} M_f + \frac{t_S}{t_T} M_s \qquad (3.2)$$

where the subscripts *T*, *s*, and *f* designate the total, substrate, and film respectively. This allowed for direct comparison between the modulus data obtained from free standing film tests to the composite membrane tests. Conversion from the biaxial modulus (*M*) to the Young's modulus (*E*) can be performed using

$$M = \frac{E}{1-\nu} \qquad (3.3)$$

where ν is Poisson's ratio which was assumed to be 0.25. The elastic modulus of the CuNb films tested using this method (i.e. from Fig. 3) was 131.9 ± 7 GPa. Results of these tests were consistent with the bulge test data of the free standing films and fell within the standard deviation presented. While testing of the membranes to this point has been based solely on determination of the elastic properties of these materials, it is emphasized that these linear elastic analyses become invalid once the material deforms plastically.

3.4 Nanoindentation

Using an oscillation technique to determine the contact stiffness during the indentation (a process referred to as the "continuous stiffness method"[19,20]) the elastic modulus and hardness was measured for each film. For all films tested, six to ten indentations were made several mm's away from the fabricated windows. All measurements were taken using a Berkovich diamond tip indenter, the area function used

was determined by calibration in fused quartz. To determine the modulus and hardness, the properties were assessed at an indentation depth of 5% of the film thickness to eliminate substrate effects. Figure 3.4 shows the hardness as a function of penetration depth for the CuNb film, and exhibits the range of indentation penetration depth over which the properties were effectively uniform.

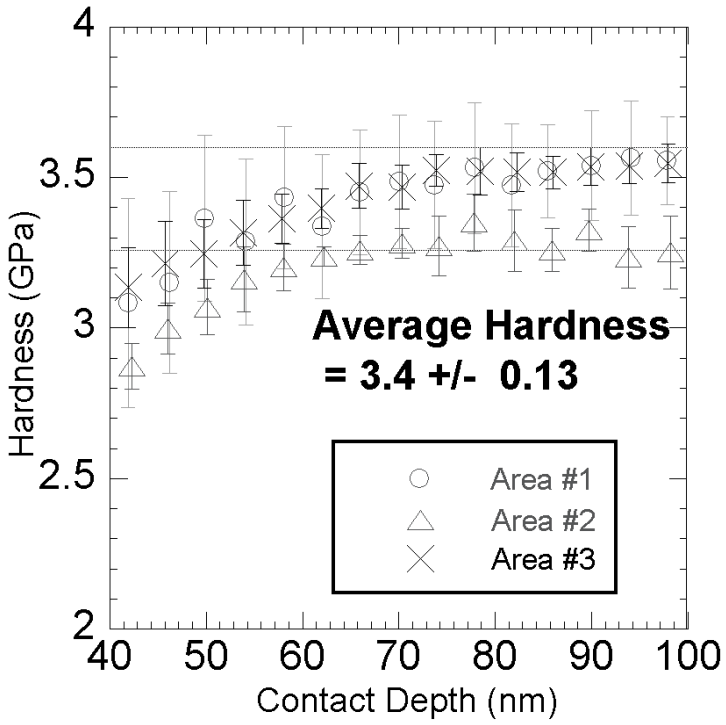

Figure 3.4- A plot of hardness measured using continuous stiffness indentation performed on the CuNb multilayer films with individual layer thickness of 20nm. Each data set shown represents an averaged set of 7-10 indents measured from different areas of the wafer.

The tabulated results of the elastic modulus determined from indentation and bulge testing are found in Table 3.2. In general the nanoindentation results were similar to the bulge testing data, showing good agreement between the two methods.

Table 3.2 Experimentally measured elastic properties of metallic multilayers

Sample	Bulge Test Modulus GPa)	Nanoindentation Modulus (GPa)
CuNb	122.6 ± 13.6	117.3 ± 2.8
CuNi	128.8 ± 9.5	115.9±12.3
CuNbNi	126.5 ± 12.6	108±3.7

3.5 Plastic Deformation of Metallic Multilayers in Tension

Rectangular Geometry

Bulge testing of a rectangular free standing membrane with an aspect ratio greater than 4 provides a uniaxial stress state in the center of the membrane; this has been used by other researchers to determine the tensile flow stress behavior of thin metallic films. [8,10,11,12,17] Though limited to small deformations, calculation of the stress-strain relationship for a high aspect ratio rectangular membrane is fairly straightforward. [12,10] The stress and strain in the rectangular membrane are uniform across the entire width of the membrane and independent of whether the film deforms elastically or plastically, they can be related to the applied pressure *P*, out of plane deflection *w*, and membrane geometry by

$$\sigma_{\text{Plane Strain}} = \frac{a^2 P}{2wt} \quad , \qquad \varepsilon_{\text{Plane Strain}} = \frac{2w^2}{3a^2} \tag{3.4,3.5}$$

when the deflection of the membrane is much smaller than the width.[14] Figure 3.5 shows a pressure deflection curve obtained during bulge testing of a rectangular membrane with its corresponding stress vs. strain plot.

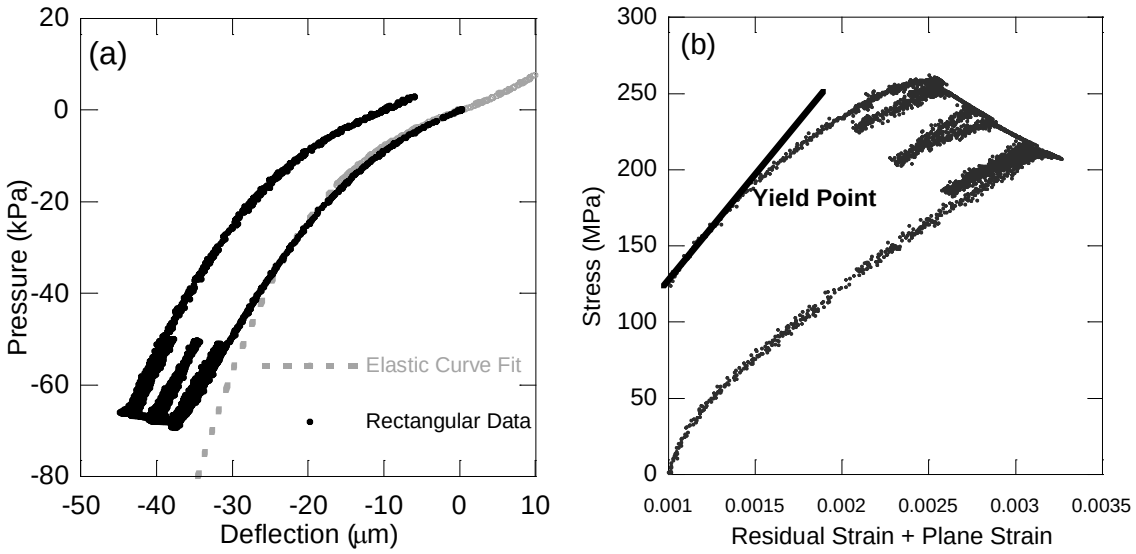

Figure 3.5- A) Pressure deflection curve showing plastic deformation. The specimen shown was loaded to a pressure of -67 kPa where the film was allowed to deform at a constant pressure. The film was then unloaded slightly and reloaded several times showing elastic unloading after repeated plastic deformation. B) The representative stress vs. strain plot calculated from A.

Inspection of the initial loading curve in Figure 3.5b compared to the unloading segments seems to suggest that varying degrees of stiffness are present in the film. However, due to the nature of bulge test measurements, there is a fourth order dependence of elastic properties on geometry. For the case of plastic deformation, it is then understandable that since an instantaneous film area was not incorporated to the calculation, the unloading of a deformed film would not have the same slope as the initial loading curve. The linear trend shown Figure 3.5b is representative of the elastic properties of the film determined by nanoindentation. While substantial plastic deformation can be seen in Figure 3.5, the subsequent values reported focus on the very onset of plasticity.

Residual stresses in the films account for a nonzero initial stress-strain state. This, in conjunction with very low maximum strains that can be applied with our current window geometry and the method of using a pressure variator for application of the pressure (the maximum applied strain in the current apparatus is approximately 0.2%-0.3%) make the incorporation of a traditional 0.2% offset strain challenging. In addition, other researchers using bulge testing to assess plastic deformation have noted that to generate a uniform strain field within nanocrystalline metals offsets as high as 0.7% should be used to ensure plastic deformation occurs in all grains[12]; the strains encountered in this study were significantly lower than this value, consistent with other bulge testing observations.[9] For this reason, measurement of the yield point was accomplished by plotting kPa/μm vs. μm^2 and identifying the point where the data can no longer fit a linear trend. [9,17,21-24] The yield pressure measurement was then recorded at a 5% pressure offset (~.01% strain offset). To ensure accuracy of the measurement, the plastic pressure deflection curve of each sample was also plotted against an extrapolated curve fit of its elastic measurements and is shown in Figure 3.5a. Deviation of the plastic curve from the extrapolated elastic fit was shown to be consistent to within ± 4kPa of the yield pressure value found from kPa/μm vs. μm^2 plot.

For metallic materials that have moderate to low yield stress to modulus ratios it is widely accepted that the indentation hardness is approximately a factor of three times the flow stress, σ_f (more specifically $\sigma_f = H/2.8$).[25,26] Using this concept, the flow stress values should range from 0.6GPa for the CuNi to 1.1GPa for the CuNb.

The nanoindentation results show that the CuNb films exhibited the highest hardness. For this reason, with the yield stress and strain now well defined, calculation of a strain hardening exponent was performed on rectangular specimens as modeled by Vlassak.[14] For a rectangular membrane with aspect ratio greater than or equal to 4, the strain hardening coefficient (n) is given by

$$\frac{\sigma}{\sigma_y} = \left(\frac{\varepsilon}{\varepsilon_y} \right)^n \quad \text{for} \quad \sigma > \sigma_y \tag{3.6}$$

Data from the ten CuNb rectangular specimens was used for this calculation. The strain hardening exponent at a 10% pressure offset was 0.87±.08 for the CuNb films which is significantly higher than the bulk value of .35-.4 for copper.[27] However it should be noted that because only very small strains were achieved, it is most likely that deformation occurred in localized zones over the membrane. While this technique only provides a first order estimate, it does demonstrate that these materials have the potential to exhibit very high strain hardening properties.

Square Geometry

Because the most accurate representation of a yield point measurement is identified through the experimental measurements, kPa/μm vs. μm^2 plots were also used to identify the pressure at which yield first occurred for the square geometry. A summary of the yield pressures for all membrane geometries is presented in Table 3.3. For a square membrane, calculation of the stress and strain is not as simple as the rectangular case due to the biaxial stress state. As modeled by Hoelfelder [17] using the Timoshenko/Vlassak

energy minimization method, the Von Mises stress and strain at the center of an elastically loaded square membrane can be calculated as.

$$\sigma_{square} = f(v) \cdot \frac{E \cdot h^2}{a^2} \tag{3.7}$$

$$\varepsilon_{rect} = \varepsilon_o + f(v) \cdot \left(\frac{Pa}{Et} \right)^{2/3} \tag{3.8}$$

where *f(v)* is a function of Poisson's ratio.17. It should also be noted that the stress from (7) will be a slight overestimate the yield stress due to the fact that a 5% pressure offset was incorporated.

Because all experimental measurements reported in this paper describe the deflection of the center of the membrane it is important to account for any edge effects and non-uniform stress states. For this reason, ABACUS models were created for the rectangular and square membranes. Modeling of these films was performed in a manner similar to that of Reddy and Kahn [28] and was found to yield similar results. Using these models, the stress at the center of the membrane can be described as a fraction of the highest stress encountered by the film. This allows for determination of the maximum stress within the membrane when only the stress at the center of the membrane is known. Using the Von Mises yield criterion, Figure 3.6 shows the highest normal stresses encountered in the square membrane are at the mid sections of the edges.

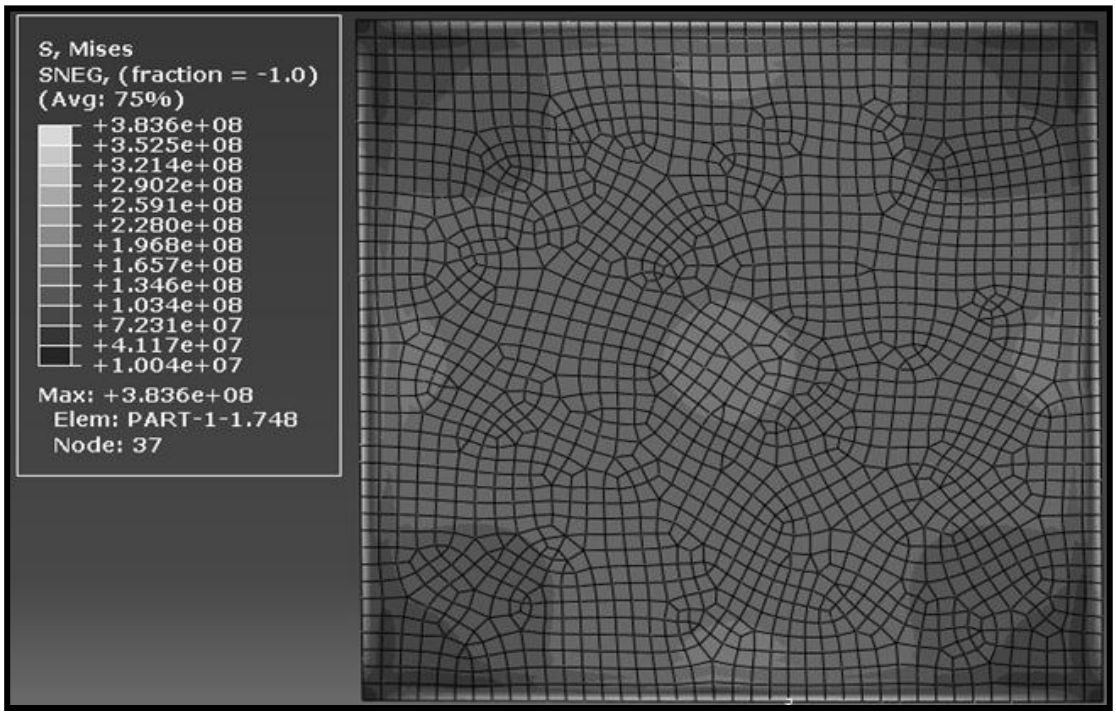

Figure 3.6 - FEA results showing the Von Mises Stresses present in a square membrane with side length 4mm.

Incorporating a 15μm offset at the edge of the membrane to alleviate constraint conditions (by St. Venant's Principal), the ratio of highest stress in the membrane to the stress at the center of the membrane was found to be 1.92 for square membranes and 2.16 for rectangular membranes. The stress ratio changes slightly depending on the applied pressure. This error was addressed by modeling the membrane at the average yield pressure determined by bulge testing, and using the ratio at that yield pressure. With these values, the highest applied stress in the film at the point of first yield was calculated and is shown in Table 3.3 for all material and geometry combinations.

Table 3.3 Plastic properties of multilayer films, including hardness, the onset of yielding, and the maximum stress in the membrane at the point of first yielding.

Sample	Hardness (GPa)	Applied yield Pressure (kPa)	Biaxial Stress at yield, Center of the membrane (MPa)	Edge Stress (MPa)
CuNb Rectangle	--	31.0± 7.1	192.7 ± 27	416.2
CuNb Square	3.4±.13	49.5 ± 8.4	222.3 ± 24	426.8
CuNi Square	1.9±.24	43.3±4.0	254.6±10.6	488.8
CuNbNi Square	2.3±.11	39.1±5.6	200.4± 2.5	384.8

While the maximum stress in the membrane at the onset of yield is significantly lower than the predicted flow stress that would be expected from the hardness data, an important source of this deviation is that the values reported in Table 3.3 are for the onset of plasticity; not for uniform deformation over the membrane. Yielding for all of the systems tested was shown to occur at similar stress values. The non-uniform deformation within a membrane, and the challenges with nanocrystalline materials achieving uniform strain throughout the sample are likely responsible for the difference between hardness and initial yield behavior. However, the particularly interesting trend is that the hardest samples do not have the highest initial yield stress. This suggests that hardening must have a significant role in the plasticity of the samples at increasing strains. Similarly, for future fatigue testing, if tests are to be carried out prior to the onset of dislocation motion, stresses significantly lower than one third of the hardness should be chosen for the testing conditions.

3.6 Conclusions

The mechanical properties of CuNi, CuNb, and CuNbNi films were assessed using complementary testing methods of bulge testing and nanoindentation. Tri-layer films have a hardness that is between that of the bi-layer films; all films have similar elastic modulus values of approximately 125 GPa. The onset of microscale yielding has been identified using the bulge testing technique, and occurs at stresses approximately 50-70% of that which is expected from the hardness data, even when corrected for the localized stresses using estimations of the stress concentration based on a finite element analysis. The differences between the flow stress and onset of plastic deformation are likely related to both the non-uniform stress state and the strain hardening behavior of these multilayer films. The samples which exhibit the highest hardness do not correspond to the highest initial yield strengths and as such future high cycle fatigue testing should be carried out at stresses low enough to minimize dislocation motion.

3.7 Acknowledgements

The authors wish to acknowledge the financial support of the Office of Basic Energy Science at the US Department of Energy under grant number DE-FG02-07ER46435. The assistance of Dr. A. Misra of Los Alamos National Laboratories for growth of the Cu/Nb and Cu/Nb/Ni films is greatly appreciated.

3.8 References

[1] Misra, A., Kung, H., 2001, "Deformation behavior of nanostructured metallic multilayers," Adv. Eng. Materials, **3**, pp. 217-222.

[2] Wang, Y.C., Misra, A., Hoagland, R.G., 2006, "Fatigue properties of nanoscale Cu/Nb multilayers," Scripta Mat., **54**, pp. 1593-1598.

[3] Zhang, X., Hammon, D., Hoagland, R.G, Misra, A., 2005, "Work hardening in rolled nanolayered metallic composites," Acta Mat., **53,** pp. 221-226.

[4] Zhang, X., Li, N., Anderoglu, O., Wang, H., Swadener, J.G., Hochbauer, T., Misra, A., Hoagland, R.G., 2007, "Nanostructured Cu/Nb multilayers subjected to helium-ion irradiation," Nuclear Instruments & Methods in Physics Research Section B, **261**, pp. 1129-1132.

[5] Edwards, R.L., Coles, G., Sharpe, W.N., 2004, "Comparison of tensile and bulge tests for thin film silicon nitride," Experimental Mech., **44,** pp. 49-54.

[6] Mara, N.A., Bhattacharyya, D., Hoagland, R.G., Misra, A., 2008, "Tensile behavior of 40 nm Cu/Nb nanoscale multilayers," Scripta Mat, **58**, pp. 874-877.

[7] Bonnotte, E., Delobelle, P., Bornier, L., 1997, "Two interferrometric methods for the mechanical characterization of thin films by bulge tests," J. Mat. Res., **12**, pp. 2234-2247.

[8] Vlassak, J.J., Nix, W.D., 1992, "A new bulge test for the determination of young's modulus and poisson's ratio of thin films," J. Mat. Res., **7**, pp. 3242-3249.

[9] Small, M.K., Daniels, B., Clemens, B., Nix, W.D., 1994, "The elastic biaxial modulus of ag-pd multilayered thin films measured using the bulge test," J. Mat. Res., **9**, pp. 25-30.

[10] Kalkman, A.J., Verbruggen, A.H., Janssen, A.M., Groen, F.H., 1999, "A novel bulge test setup for rectangular free standing thin films," AIP Rev., **70**, pp. 4026-4031.

[11] Wei, X., Lee, D., Shim, S., Chen, X., Kysar, J., 2007, "Plane strain bulge test for nanocrystalline copper thin films," Scripta Mat., **57,** pp. 541-544.

[12] Kraft, O., Volkert, C., 2001, "Mechanical testing of thin films and small structures," Adv. Eng. Mat., **3**, pp. 99-109.

[13] Kennedy, M.S., Olson, A.L., Raupp, J.C., Moody, N.R., Bahr, D.F., 2005, "Coupling bulge testing and nanoindentation to characterize materials properties of bulk micromachined structures," Microsystem Tech., **11,** pp. 298-302.

[14] Xiang, Y., Chen, X., Vlassak, J.J., 2005, "Plane strain bulge test for thin films," J. Mat. Res. **20**, pp. 2360-2370.

[15] Misra, A., Hirth, J.P., Hoagland, R.G., 2005 "Length scale deformation mechanisms in incoherent metallic multilayered composites," Acta Mat., **53,** pp. 4817- 4824.

[16] Foecke, T., Kramer, D.E., 2003, "In situ TEM observations of fracture in nanolaminated metallic thin films," I. J. Fracture, **119**/**120**, pp. 351-357.

[17] Hohlfelder, R.J., 1999, "Bulge and blister testing of thin films and their interfaces," Ph.D. thesis, Stanford University, USA.

[18] Tabata, O., Kawahata, K., Sugiyama, S., Igarashi, I., 1989, "Mechanical property measurements of thin films using load deflection of composite rectangular membranes," *IEEE Micro Electro Mechanical Systems Proceedings, An Investigation of Micro Structures, Sensors, Actuators, Machines and Robots*, pp. 152-156.

[19] Oliver W.C and Pharr, G.M., 2004, "Measurement of hardness and elastic modulus by instrumented indentation: Advances in understanding and refinements to methodology", J. Mater. Res., **19**, pp.3-20

[20] Asif, S.A.S., Wahl, K.J., Colton, R.J., 2000, "The Influence of Oxide and Adsorbates on the Nanomechanical Response of Silicon Surfaces," J. Mat. Res., **15**, pp. 546-553.

[21] Martins, P., Delobelle, P., Malhaire, C., 2007, "Comparison of bulge test and point deflection methods for the mechanical characterization of submicron thick composite membranes*" Solid-State Sensors, Actuators and Microsystems International Conference, Transducers and Eurosensors*, pp. 379-382.

[22] Mitchell, J.S., Zorman, C., Kicher, T., 2003, "Examination of bulge test for determining residual stress young's modulus and poisson's ratio of 3C-SiC thin films," J. Aerosp. Eng., **16**, pp. 46-54.

[23] Leondes, C.T., 2006, "Techniques in residual stress measurement for mems and their applications," *MEMS/NEMS Handbook,* Springer, USA.

[24] Jankowski, A.F., Tsakalakos, T., 1996, "Effects of deflection on bulge test measurements of enhanced modulus in multilayered films" Thin Solid Films, **290**, pp. 243-247.

[25] Tabor, D., 1951, *The Hardness of Metals*, Oxford Clarendon Press, USA.

[26] Sundararajan, G., Tirupataiah, Y., 2006, "The Localization of Plastic Flow under Dynamic Indentation Conditions: I. Experimental Results," Acta Mat., **54**, pp. 565-575.

[27] Hertzberg, R.W., 1996, *Deformation and Fracture Mechanics of Engineering Materials 4th edition*, Wiley & Sons. Inc., USA.

[28] Reddy, A., Kahn, H., Heuer, A., 2007, "A MEMS-based evaluation of the mechanical properties of metallic thin films," J. Microelectromechanical Sys., **16**, pp. 650-658.

Chapter 4 Thin Film Failure

4.1 Introduction – Deformation in Metallic Multilayers

Metallic multilayer thin films are ideally suited for studies of length scale dependent deformation. The control sequential sputtering offers, during deposition, makes tailoring individual layer thickness an uncomplicated process. The influence of length scales such as the layer thickness in multilayer films is an area that has gained a significant amount of attention. As discussed in Chapter 1, the effects length scale has on the plasticity of multilayer thin films can be divided into three clear deformation regimes as noted in chapter 1, and reproduced here for clarity in Fig. 4.1.[1] This model, called the Confined Layer Slip (CLS) model was developed by Misra and Hirth.

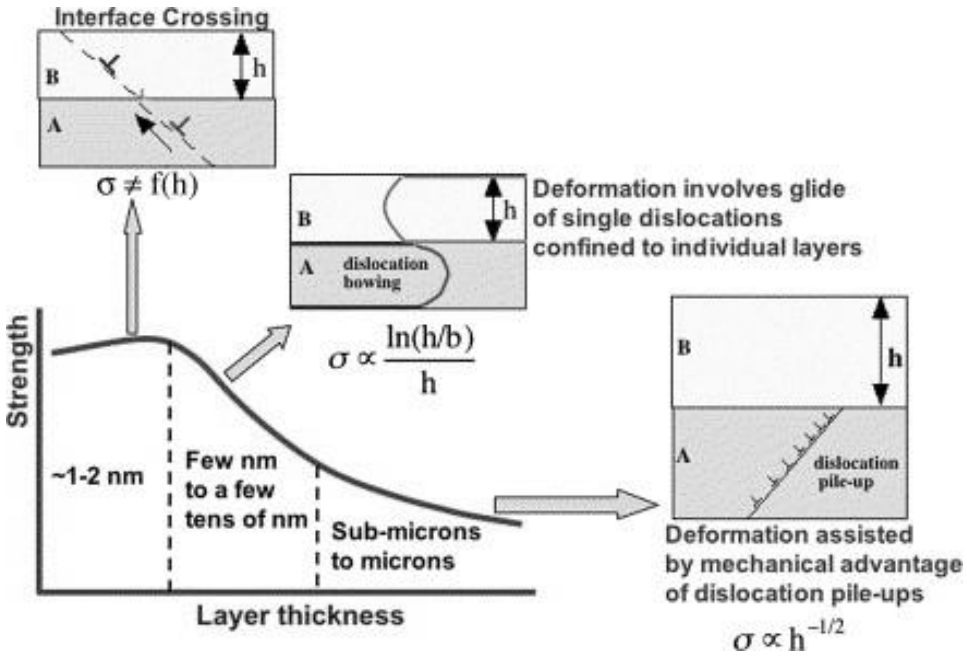

Figure 4.1- Confined Layer Slip model showing the effects of layer thickness on strength.[1]

At layer thicknesses in the micron range, deformation follows the well known Hall Petch dependence, with strength increasing as the layer thickness/grain size decreases. Decreasing the grain size leads to an increase in the number of grain boundaries, hindering dislocation motion. However, this effect breaks down as individual layer thicknesses are further reduced, to the extent that in the 1-2nm layer range, the predominant mode of deformation is identified as interface cutting.[1]
In the "few tens of nm" range, which we are concerned with for this study, the layer thickness is so small that only the motion of one dislocation at a time can occur. The Orowan stress for the motion of a glide dislocation confined in one layer is still small relative to the stress needed for a single glide dislocation to transmit across the interface.[2] Hence, plasticity initiates by the motion of Orowan loops is confined within one layer.[1,2] Over the range that this mechanism is operative, decreasing the individual layer thickness increases the required Orowan stress to move the dislocations leading to a strengthening effect of the multilayer.

Typical failure modes encountered in metallic multilayer thin films include cracking both along the interface and perpendicular to it, and surface initiated failures.[3-5] Surface initiated failures are caused by material instability which can be a result of stress related to film deposition, or direct external forces making it the main failure mode for these materials.[4] Evidence of the plasticity associated with these failures can be seen via scanning electron microscopy as surface kink bands[4] and damage bands[6] formed near the material surface, necking or delamination between layers.[7]

While the majority of measurements on multilayer films have been carried out using nanoindenation, in this study Cu/Nb, Cu/Ni and Cu/Nb/Ni multilayer failures via burst testing were investigated. A traditional bulge testing set-up equipped with a nitrogen gas tank was required in order to reach the high pressures required to fail these multilayer films. While the yielding in Chapter 3 was shown to initiate at pressures of approximately 50kPa (stresses of ~.4GPa) which were easily reached using the pressure/vacuum variator (bellows), the pressures which were required to burst these membranes were greater than 10 times this value requiring the fabrication of a unique pressurization vessel/compressed air system for testing these specimens.

4.2 Procedures

The multilayer films tested in this work were deposited at Los Alamos National Labs by sequential DC magnetron sputtering. Layer thicknesses were 20nm for Cu, Ni, and Nb with a total film thickness reaching approximately 2 μm. The sample substrates were boron doped and oxidized, with a 2 μm boron doped layer and a thermally grown oxide on the order of 150 nm. The different window geometries were created with standard photolithography techniques. Square films dimensions were 4mmx4mm, and rectangular specimens were 1.5mmx 10mm. Circular windows were fabricated using Deep Reactive Ion Eteching (DRIE) and had diameters of 3mm to 4mm. Reactive Ion etching was used to remove the substrate backing for testing of the free standing films.

During bulge testing, measurement of the film displacement at the center of the membrane was performed with the use of a Polytec OFV 511 scanning laser vibrometer.

Pressure was applied to the membrane using a standard pressure regulator coupled with a compressed gas cylinder of nitrogen. As discussed in Chapter 3, because of the high yield strength but low adhesion strength of these films, mounting orientations were chosen to eliminate the problem of film delamination during testing. Although, even using the testing orientation shown in Figure 4.2, it can be seen that very weak film-substrate interfaces can still play a role.

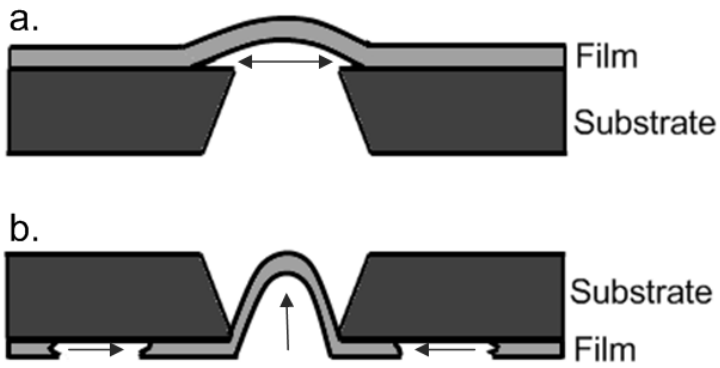

Figure 4.2 – Films with very poor adhesion fail by a) traditional delamination where the arrow shows where the film has left contact with the substrate and b) tearing and sliding off of the substrate as opposed to deforming over the window region.

The failure mode shown in Figure 4.2b was only witnessed for CuNi samples that were tested. Because of the very poor adhesion of these films, many of which exhibited spontaneous delamination limiting the number of CuNi samples were able to be burst tested. Figure 4.3 below shows examples of samples that have undergone the respective failures shown in Figure 4.2.

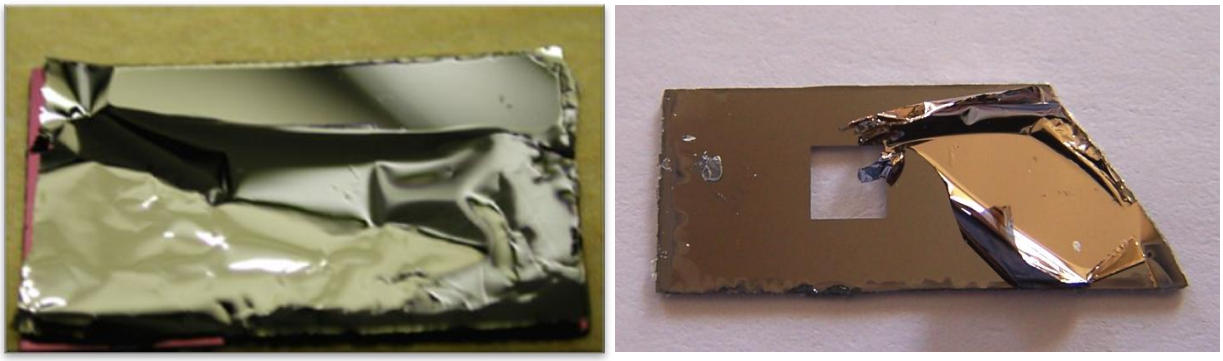

Figure 4.3 – Thin film samples exhibiting 4.2a-delamination (left) and 4.2b delamination (right). The silicon substrate showing in the image at right was completely covered by the multilayer film before testing. The remaining film is what was left after the rest of the film delaminated and was pushed through the window opening.

While several of the films encountered failed by delamination, the following work presented deals only with films which did not exhibit such poor adhesion. The goal of this chapter was to gain a more thorough understanding of the deformation occurring in these multilayer films systems after the initial yield outlined in Chapter 3.

4.3 Results

4.3.1 Thin Film Gold

Preliminary testing was performed on thin film gold samples with the goal of acquiring pressure deflection curves which showed evidence of plastic deformation which could then be compared to the multilayer films being tested. Eight thin film gold samples, 2 rectangular and 6 square were tested until failure. Gold samples were measured by scanning electron microscopy and shown to be 0.75μm thick with a grain size of ~85nm as measured using ImageJ and seen in Figure 4.4. It should be noted that for the grain size calculation, it is assumed the grains are circular in geometry.

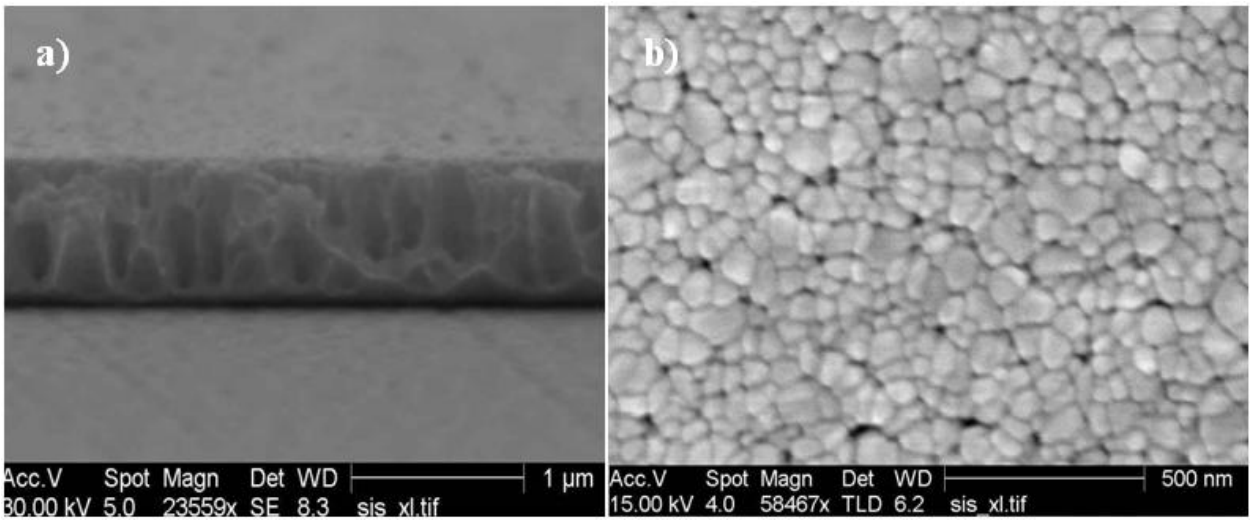

Figure 4.4- SEM images of sputter deposited gold films showing a) thickness and b) grain size.

Comparing the initial parts of the pressure vs. deflection curves as seen in Figure 4.5, the gold films were substantially more compliant than any of the multilayer systems tested, which is to be expected of the thinner .75µm gold film as compared to the thicker 2µm multilayers.

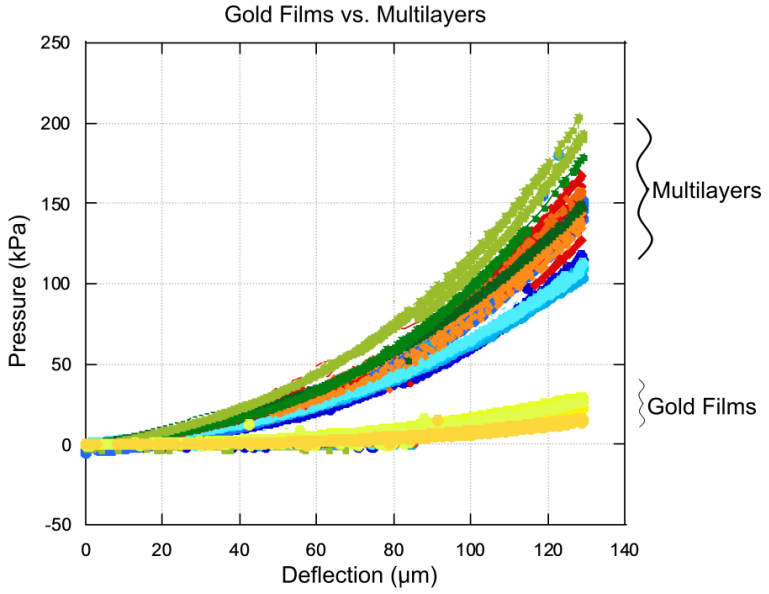

Figure 4.5 – Pressure vs. Deflection curves comparing the multilayer films to the more compliant gold films.

For a sample set of 8 thin film gold specimens, the Young's modulus was calculated to be 71.52 ± 12.38 GPa with a residual stress of 41.6 ± 10.9 MPa, which correlates well to the modulus values reported in literature. [8-10] Values for modulus and residual stress were calculated using the standard bulge equation given by:

$$P = Ah + Bh^3 \qquad \text{Eqn. 4.1}$$

A and *B* can be determined by curve fitting the pressure deflection data and solving for the modulus and residual stress in the film.

$$A_{curve\ fit} = \frac{C_1 \sigma_o t}{a^2} \qquad \text{Eqn. 4.2}$$

$$B_{curve\ fit} = \frac{C_2 E t}{a^4 (1-\upsilon)} \qquad \text{Eqn. 4.3}$$

Where a is one half of the side length, t is the membrane thickness, E is Young's modulus, υ is Poisson's ration, σ is the residual stress and constants C_1 = 3.4 and C_2 = 1.84 for square membranes or C_1 = 2 and C_2 = 4/[3(1+υ)] for rectangular membranes. Table 4.1 below shows a comparison of the elastic modulus of the multilayers compared to that of the gold. A poisson's ratio of .42 was used for the gold[11], while a value of .25 was assumed for the multilayer films.

Table 4.1 Experimentally Determined Modulus Values determined by Bulge Testing.

Sample	**Bulge Test Young's Modulus (GPa)**
Gold	61.4 ± 6.3
CuNb	122.6 ± 13.6
CuNi	128.8 ± 9.5
CuNbNi	126.5 ± 12.6

The respective pressure/deflection curves of the gold films showed substantial plastic deformation, with side length increases during deformation of 40-80μm depending on the geometry. Figure 4.6a-b illustrates the deformation seen in the pressure deflection curves of square and rectangular samples.

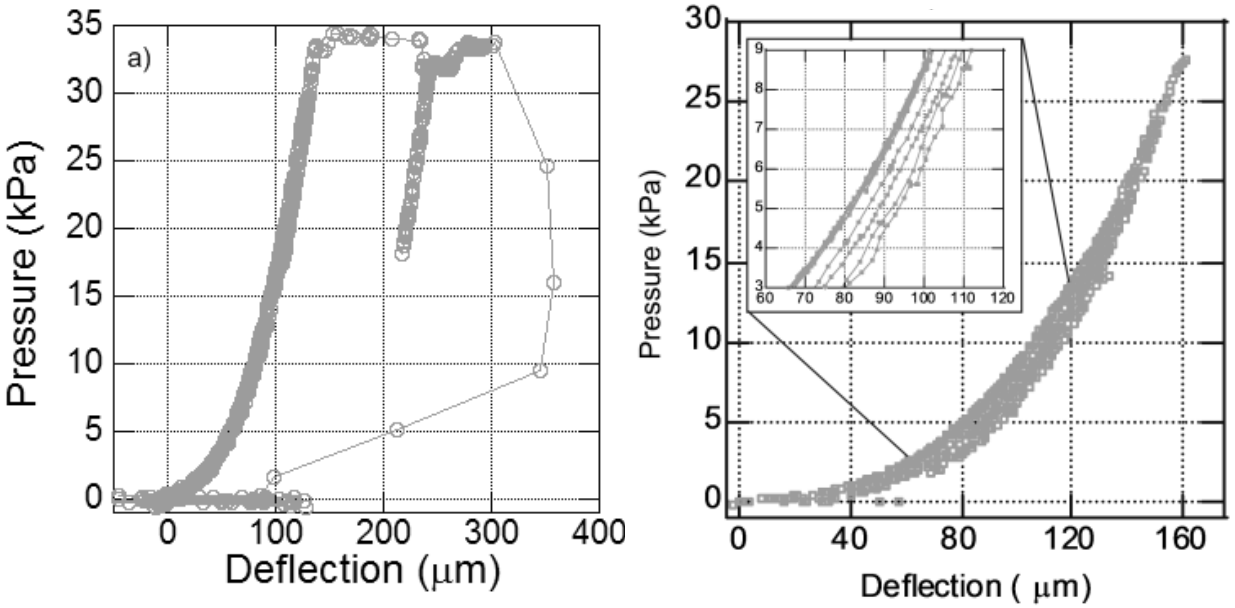

Figure 4.6 – Pressure vs. Deflection Curves for .75μm Gold a) square geometry showing ~80μm of deformation before failure and b) rectangular geometry showing ~30μm deformation.

The square film is shown to reach much higher deflections due to plastic deformation compared to the rectangular film. This is purely a size effect, seen because the square membranes have much larger dimensional constraints (4mm) than the rectangular samples (1.5mm). In addition, if the pressure is applied too rapidly to the free

standing gold membranes, they will burst on the loading curve. For this reason, gold films were pressurized slowly in order to capture the plastic yielding seen in Figure 4.6a.

When bulge testing, plotting kPa/μm vs. μm^2 is commonly used in place of a stress vs. strain curve for square geometry films to show deviation from linear elasticity.[12-17] This method has been widely utilized by several researchers, and is simply a linearized fit of the standard bulge equation, Equation 4.4

$$P = Ah + Bh^3 \qquad \text{Eqn. 4.4}$$

$$\frac{P}{h} = A + Bh^2 \qquad \text{Eqn. 4.5}$$

$$y = b + mx \qquad \text{Eqn. 4.6}$$

When plotted, the y-intercept is then proportional to the residual stress in the film and the slope is proportional to the modulus. This method of analysis was used on the square film geometry while stress and strain calculations were performed for rectangular specimens. Figure 4.7 shows an example of a kPa/um vs. um^2 plot for a gold specimen. Several unloading and reloading sequences were performed until the film failed. The solid line shows the initial loading and unloading curve, where deviation from this line indicates yielding. The sharp drop in the data seen at failure is due to film rupture.

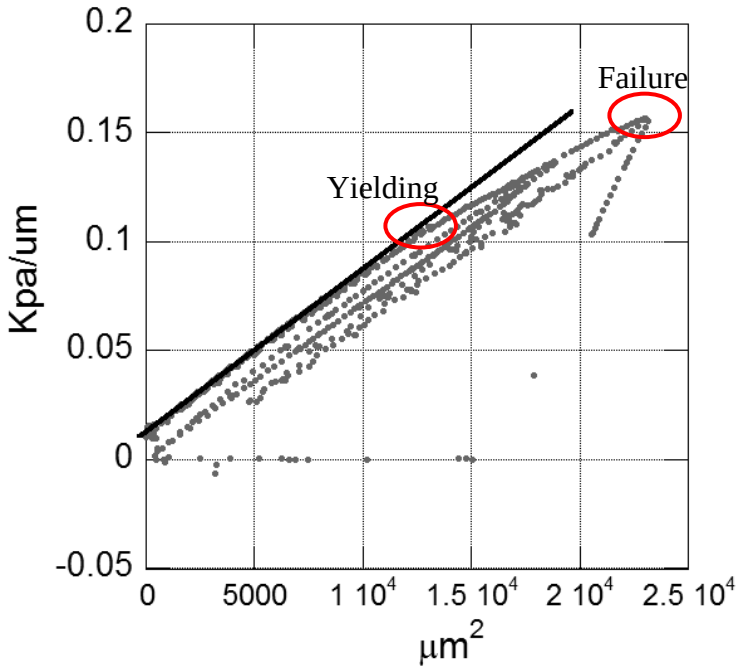

Figure 4.7 – kPa/µm vs. µm2 plot of a .75µm thick gold film. Several loading and unloading sequences were performed showing deformation of the film.

Rectangular gold films were also tested so that the stress strain behavior of these films could be seen. Figure 4.8 below shows one such plot.

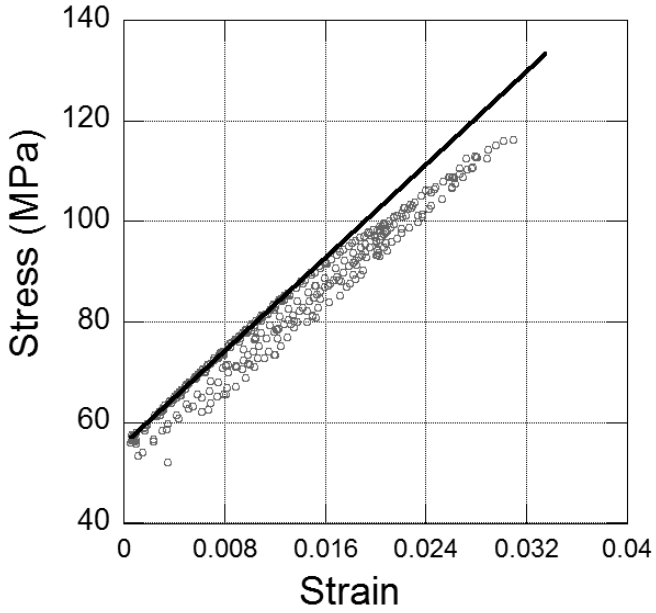

Figure 4.8 – Stress vs. Strain Plot for rectangular specimen of .75µm gold

For a sample set of six square membrane gold films, yielding was found to initiate at 11.5 ± 4.2 kPa which equated to stresses of approximately.12GPa, while burst pressures were found to be 36.8 ± 10.8kPa. A summary of these values and their respective yield stresses can be seen in Table 4.2.

4.3.2 Multilayers

A total of 18 multilayer samples were tested to failure, six of each film system contribute to the data shown. Yielding of the square window geometry can be seen for all multilayer systems in Figure 4.9. As shown in these plots, the CuNi films were able to withstand the highest ultimate stresses, while the yield stresses for all films were shown to be very similar. All films data shown in Figure 4.9 ruptured at or near the peak values shown.

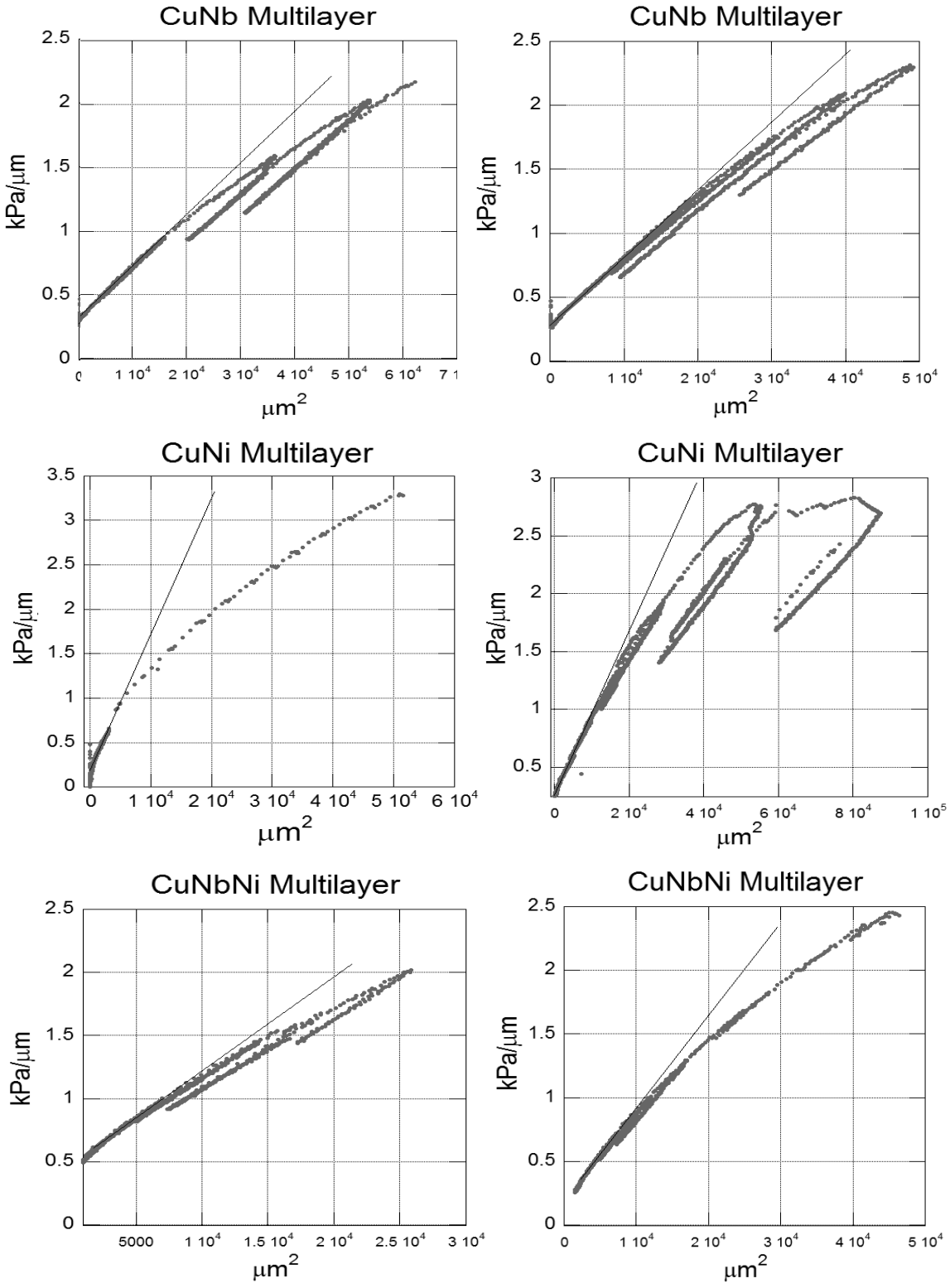

Figure 4.9 – Multiple kPa/μm vs. μm^2 plots of the multilayer films showing deviation from linearity and substantial plastic deformation before failure. Lines drawn in are reference points showing the curve fit of the first few data points before deformation.

A summary of the mechanical properties of these films from bulge and burst testing is included in Table 4.2 below.

Table 4.2 Comparison of Experimental Data Gathered from Freestanding Square Films

Sample	Applied yield pressure (kPa)	Biaxial stress at yield, Membrane center (MPa)	Edge stress at yield (MPa)	Hardness (GPa)	Burst Test Failure Pressure (kPa)
Gold	11.5 ± 4.2	119.8 ± 14	249.2	n/a	36.8 ± 10.8
CuNb	49.5 ± 8.4	222.3 ± 24	426.8	3.4±.13	393.0 ± 93.0
CuNi	43.3±4.0	254.6±10.6	488.8	1.9±.24	624.7 ± 89.6
CuNbNi	39.1±5.6	200.4± 2.5	384.8	2.3±.11	372.3 ± 48.2

Analysis of the films via electron microscopy and optical microscopy was also performed on specimens which were burst tested and showed a significant amount of plastic deformation. Evidence of ductile failure was seen in failed samples, and plastic deformation prior to film rupture was shown to be localized at the centers of the edges, as predicted by the finite element model in Chapter 3. The images shown in Figure 4.10 show evidence of the yielding which was observed.

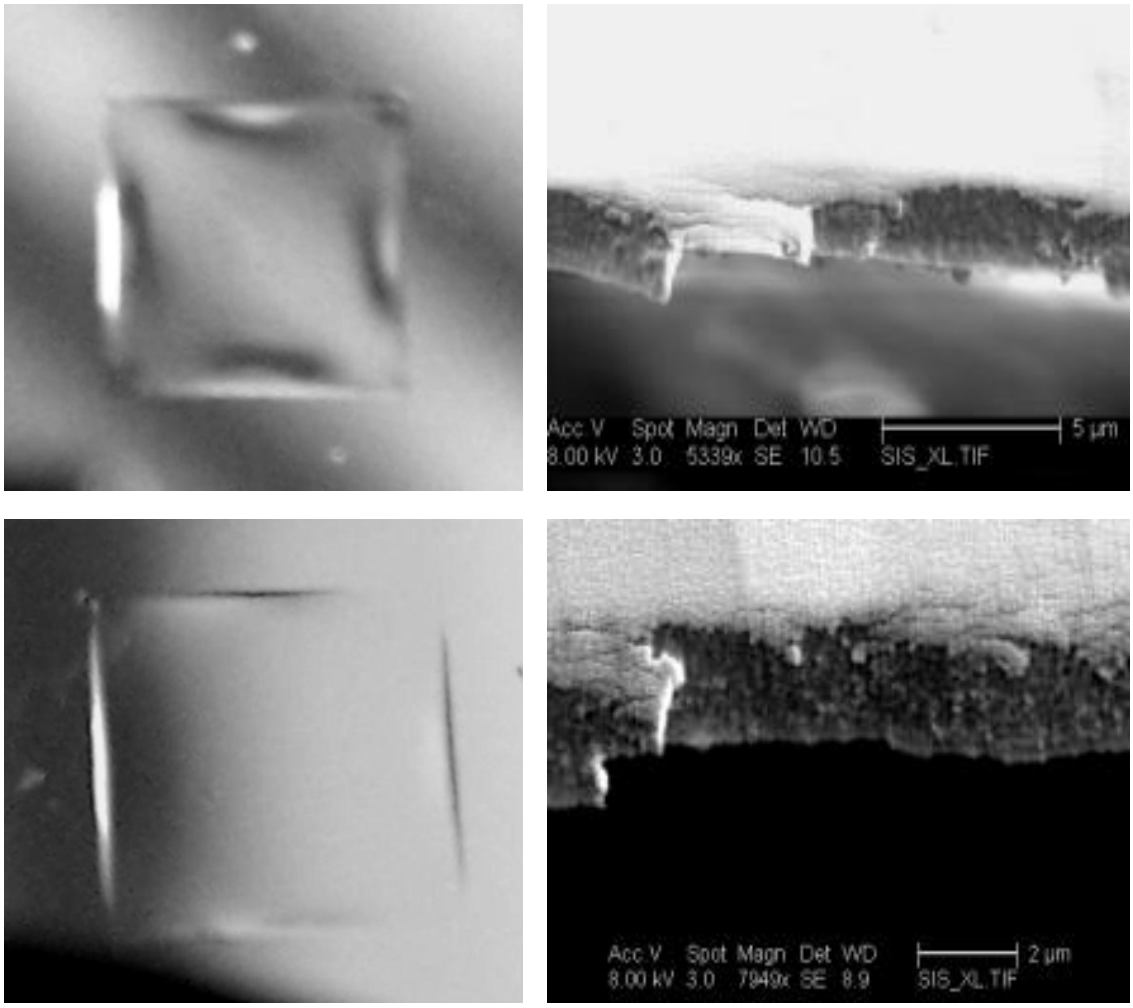

Figure 4.10 – Images on the left are optical photographs showing elongated regions of the film while still attached to the substrate window. SEM images are shown at right depicting dimpled fracture surfaces and some necking.

Analysis of the curves in Figure 4.8, in addition to the elastic modulus and yielding outlined in Chapter 3, led to a pictographic prediction of the full stress vs. strain and hardening ability of these materials as shown in Figure 4.11.

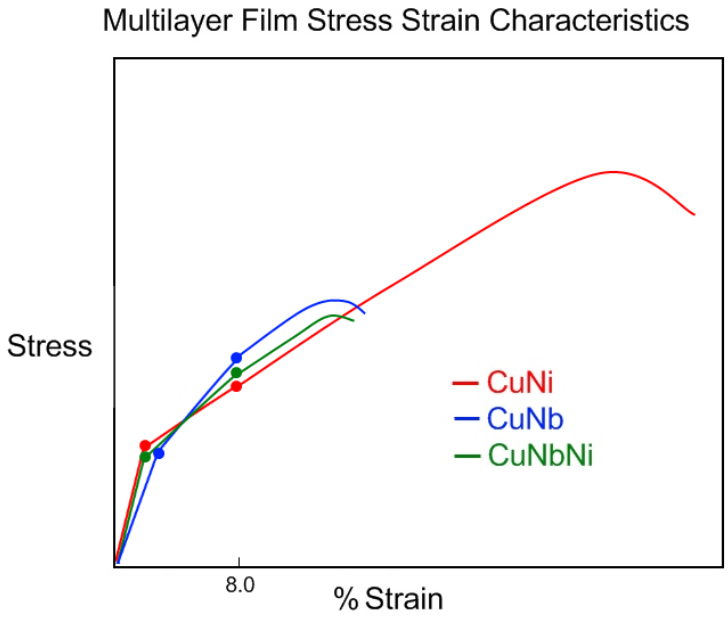

Figure 4.11 – Prediction from analyses performed in Chapters 3 and 4 showing behavior of the full stress vs. strain curve for the multilayer films of interest, properties have been exaggerated for visual purposes.

A summary of the information presented in this prediction is found in Tables 4.1 and 4.2, much of which was identified in Chapter 3. Yielding was measured via bulge test measurements has a deviation from linearity and information on the hardness as measured by nanoindentation was used to approximate values for the flow stress, $\sigma_{flow,}$ using the Tabor relation[18,19] where;

$$\sigma_{flow} = \frac{Hardness}{2.8} \qquad \text{Eqn. 4.7}$$

In an effort to test the validity of this prediction, rectangular membranes for each of the film systems were tested and corresponding stress vs. strain plots were created. A plot comparing the stress vs. strain of the multilayer films is shown in Figure 4.12.

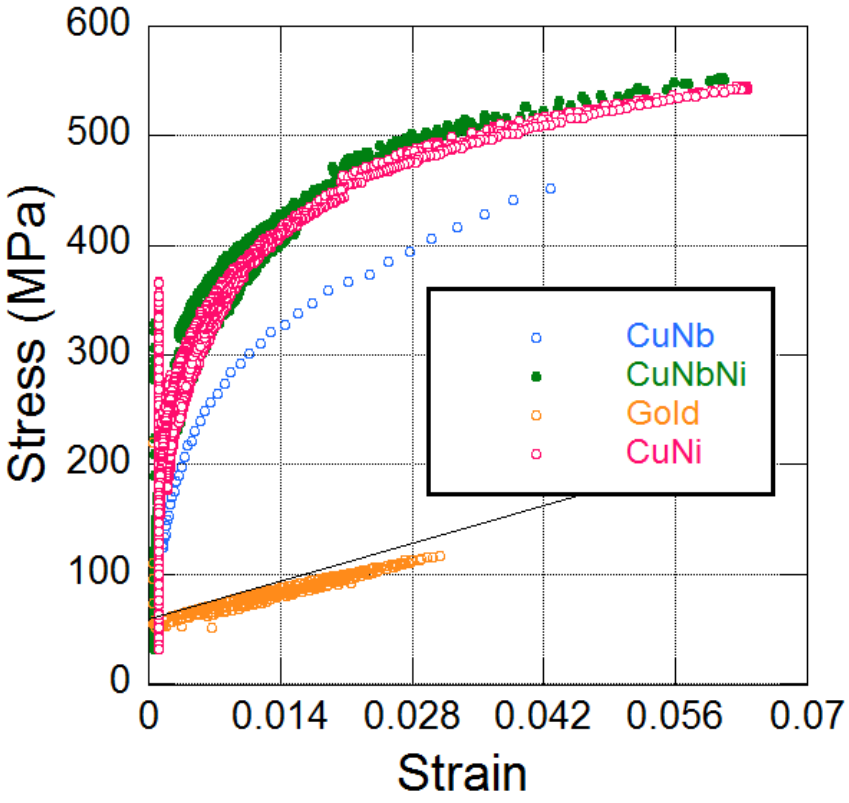

Figure 4.12 – Stress vs. Strain plots created from pressure deflection curves of rectangular films. Gold plot is also shown in Figure 4.8.

While a large portion of the stress vs. strain curves is shown in Figure 4.12, it should be noted that due to experimental limitations the stress strain curves for the multilayer films stop before failure of the rectangular samples occurred. The gold film shown did fail at a strain of 31% and a stress of Mpa. However, for the case of the multilayer films with did not reach failure, from observation of the strain values reached during testing, it is easy to see that these results are limited to the initial region of

yielding on the predictive model. Comparing the low strain regions of the curves, a very reasonable agreement between experimental data and the model is shown in Figure 4.13.

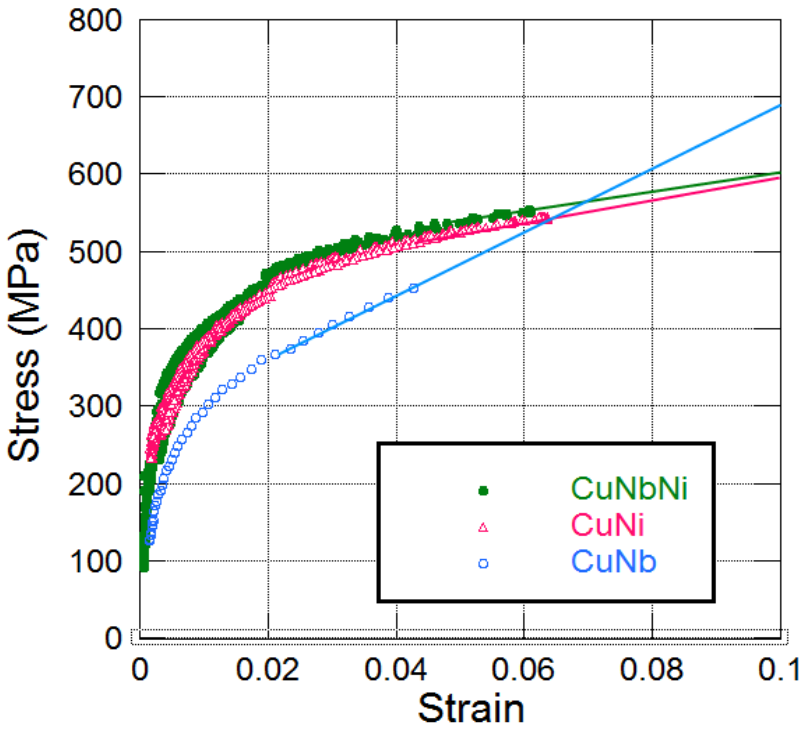

Figure 4.13 – Extrapolated stress vs. strain results obtained by bulge testing of a rectangular membrane

As seen in Figure 4.13, extrapolation of the experimental CuNb curve as it reaches larger strains is projected to surpass that of CuNi and Trilayer systems as predicted in the model. Experimental observation of the CuNi and Trilayer specimens also shows very similar stress strain behavior which is also in agreement with the model. While the strains where these processes occur do not coincide perfectly, this deviation could result from the extra hydrostatic stress component that is introduced into the model

from the flow stress/nanoindentation measurement which is not present in the experimental data due to the nature of a uniaxial/rectangular bulge test experiment.

Experimental analysis coupled with a better understanding of the mechanical behaviors of these films allows for recommendations on operating stresses for future fatigue testing on the multilayer films. Because fatigue failures occur at stresses below the yield point of a material, or in the micro-yield regime where deformation is non-uniform, future testing on the fatigue properties of these films will be carried out at values lower than the identified yield points of the films. Fatigue testing in literature[20-22] has been performed at stresses from 50 to 85 percent of the yield stress. In this study, a median range of 75% of the yield stress was decided. Recommended operating stresses for fatigue testing can be found in table 4.3 below.

Table 4.3 Fatigue Testing Recommendations

Sample	Yield Stress	75% Yield Stress
CuNb	426.8 MPa	320 MPa
CuNi	488.8 MPa	366 MPa
CuNbNi	384.8 MPa	288.6 MPa

4.4 Circular Membrane Testing

Testing of circular membrane geometries was performed in an effort to eliminate stress concentrations which were present in both the square and rectangular geometries. An image of these membranes is shown in Figure 4.14.

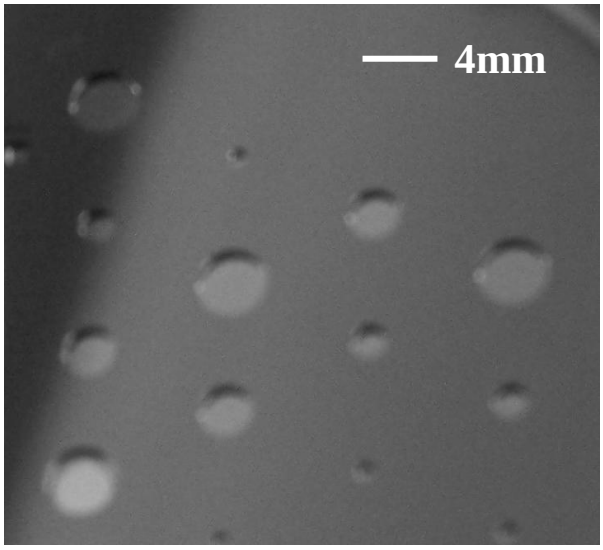

Figure 4.14 – Image taken of circular membranes used for testing.

While several different sizes of circular membranes were fabricated, with membrane diameters ranging from 1mm to 4mm, testing of these films was limited to the larger membranes due to increased deviation seen in the deflection measurement. Figure 4.15 compares the pressure deflection curves obtained by bulge testing of the different diameter circular membranes. Each graph shown includes three separate tests which were performed on each sample.

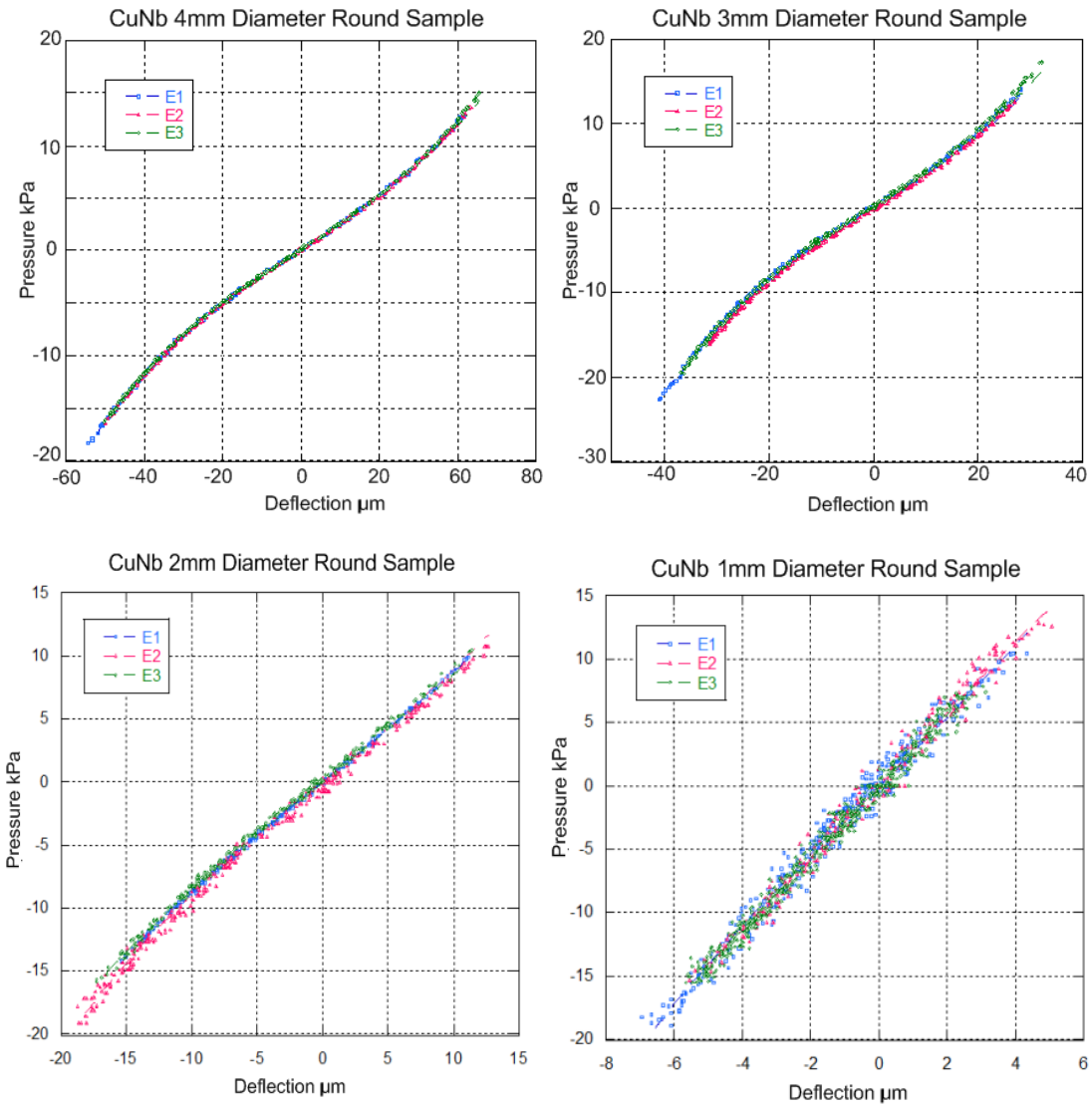

Figure 4.15 – Pressure vs. Deflection curves for different diameter circular membranes showing degradation of measurement with decreasing membrane size.

From the pressure/deflection curves shown, it can be easily seen that decreasing the membrane diameter below 3mm leads to increased deviation, in the measurement, and the cubic nature of the curve is also reduced. The calculated modulus of the 4mm diameter specimen shown was found to be 128.9GPa while the modulus of the 1mm

sample, due to the non-cubic behavior from the curve fit was calculated to be 5.5GPa. For these reasons, only the 3mm and 4mm membranes were used for further testing.

Comparison of the pressure deflection /relationships for all geometries is shown in Figure 4.16

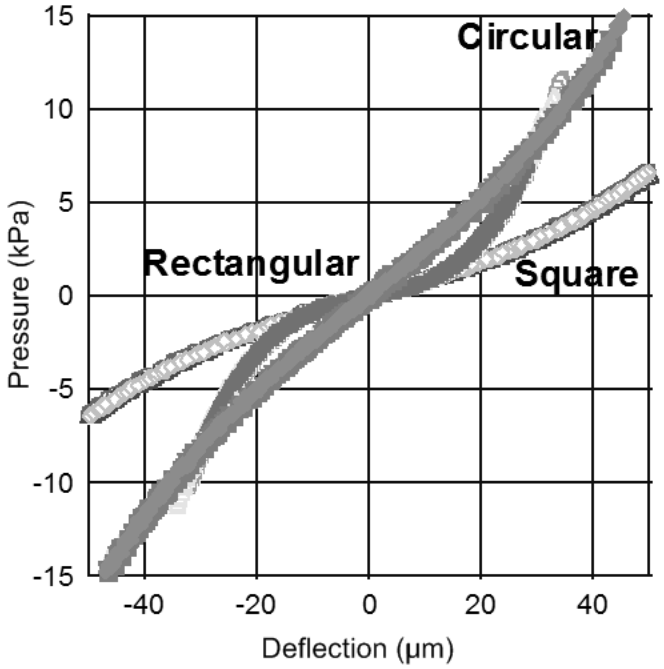

Figure 4.16 - Pressure vs. Deflection characteristics for the three different membrane geometries studied.

While the initial thought process when developing these circular membranes was to test a geometry which would eliminate the stress concentrations located at the corners of the square and rectangular membranes, it was also this effect which led to an inability to burst test any of these samples using the current test set-up. While uniform plastic deformation was seen over the surface of samples that withstood the maximum pressure (950kPa) of the current test set-up, it was the inability to rupture these films which led to their exclusion from the development of the predictive model. Stress vs. strain curves

were not able to be fabricated for these samples due to the Hookian dependence of the stress vs. strain calculations for circular films as stated in Chapter 2.

4.5 Conclusions

Significant plastic deformation was shown in CuNb, CuNi and CuNbNi multilayers with strains greater than 5% achieved before failure. Mechanical Properties testing of elastic modulus, yield point, hardness and burst pressure led to the development of a predictive model for the stress strain behavior of CuNb, CuNi, and CuNbNi multilayers. Experimental stress strain curves have shown significant agreement with the model. The development in understanding the stress /strain behavior of these materials has led to identification of appropriate operating stresses for fatigue testing these multilayer thin film systems.

4.6 References

[1] Misra, A., Hirth, J.P., Hoagland, R.G., Length-scale-dependent deformation mechanisms in incoherent metallic multilayered composites(2005) Acta Materialia **53** 4817–4824

[2] A. Misra, J. P. Hirth and H. Kung Single-dislocation-based strengthening mechanisms in nanoscale metallic multilayers," (2002) Phil. Mag. A., **82**(16) pp.2935-2951

[3] Kitamurn,T., Shibutani,T., Ueno, T., "Crack initiation at free edge of interface between thin films in advanced LSI," (2002) Engineering Fracture Mechanics **69** pp.1289–1299

[4] Wei,Y., Jiang,D., Cao,A., Zhao, H., "Surface Instability of Microscale Multilayer Thin Film Systems," (2005) Mater. Res. Soc. Symp. Proc. **854E** pp.U7.2.1-U7.2.6

[5] Freund, L.B., Suresh, S., *"Thin Film Materials Stress, Defect Formation and Surface Evolution."* 2003, Cambridge Univ. Press, USA.

[6] Ignat1,M., Lay, S., Roussel-Dherbey, F., Seguineau, C., Malhaire, C., Lafontan3,X., Desmarres, J.M., Brida, S.s "Micro Tensile Tests on Aluminium Thin films: Tensile Device and In-Situ Observations," (2009) Mater. Res. Soc. Symp. Proc. **1139**

[7] Li, X., Wei,C.,Yang, Y., "Full field and microregion deformation measurement of thin films using electronic speckle pattern interferometry and array microindentation marker method," (2005) Optics and Lasers in Engineering **43** pp. 869–884

[8] Gudlavalleti, S., Kumar, S., Anand, L., "Stress-Strain Response of Free-Standing Nano-Crystalline Gold Thin-Films," (2002) Mat. Res. Soc. Symp. Proc. **695** pp. L10.8.1-L10.8.6

[9] Wang, L., Liang, C., Prorok, B.C., "A comparison of testing methods in assessing the elastic properties of sputter-deposited gold films," (2007) Thin Solid Films **515** pp. 7911–7918

[10] Shi,J.D., Wu, K.H., Larkins, G., "A Method for Measuring the Elastic Modulus of Thin Films," (1997) Materials Characterization **38**(4-5) pp. 301-303

[11] Wilson, Jon, S., *"Sensor Technology Handbook"* Newnes, 2005.

[12] Leondes, C.T., *"MEMS/NEMS Hanbook Techniques in Residual Stress Measurement for MEMS and their Applications*," Springer, 2006, USA.

[13] Small, M. Daniels, B.J., Clemens, B.M., Nix, W.D. "The elastic biaxial modulus of Ag-Pd multilayered thin films measured using the bulge test," (1994) J.Mater. Res. **9**(1) pp.25-30

[14] Mitchell, J.S. Zorman. Christian, Kicher. Thomas. "Examination of Bulge Test for Determining Residual Stress, Young's Modulus and Poisson's Ratio of 3C-SiC Thin Films,"(2003) J. Aerosp. Engrg., **16**(2), pp. 46-54

[15] Martins, P., Delobelle,P., Malhaire, C., Brida,S., Barbier, D.,"Comparison of Bulge Test and Point Deflection Methods for the Mechanical Characterization of submicron thick composite membranes" (2007) Solid-State Sensors, Actuators and Microsystems Conference Proceedings, pp.379-382

[16] A.F. Jankowski, T. Tsakalakos. "Effects of deflection on bulge test measurements of enhanced modulus in multilayered films"(1996) Thin Solid Films, **290-291** pp.243-247.

[17] Hohlfelder, R.J., "Bulge and Blister Testing of Thin Films and Their Interfaces," Ph.D., Stanford University, 1999.

[18] Tabor, D., *The Hardness of Metals*, Oxford Clarendon Press, 1951, USA.

[19] Sundararajan, G., Tirupataiah, Y., "The Localization of Plastic Flow under Dynamic Indentation Conditions: I. Experimental Results," (2006) Acta Mat., **54**, pp. 565-575.

[20] Lee, H., Kang, S., Park, J.U., "Fatigue Strength Depending on Position of Transverse Cracks in FCAW Process," (2001) Welding Journal, pp.1-5

[21] Tan, H., "Experiment: Fatigue Testing," (2007) Online Accessed www.imechanica.com pp. 1-8

[22] Moreira, P., Richter-Trummer, V., DeCastro, P., "Fatigue Behaviour of FS, LB and MIG Welds of AA6061-T6 and AA6082-T6," *Multiscale Fatigue Crack Initiation and Propagation of Engineering Materials: Structural Integrity and Microstructural Worthiness Fatigue Crack Growth Behaviour of Small and Large Bodies*. (2008) Springer, Netherlands pp.85-111

Chapter 5 Conclusions

This work has utilized bulge testing in conjunction with nanoindentation to study the elastic properties, the onset of yielding, and failure of several multilayered film systems and geometries. CuNb, CuNi and CuNbNi multilayers with individual layer thicknesses of 20nm were studied using complementary testing methods of bulge testing and nanoindentation. Tri-layer films have a hardness that is between that of the bi-layer films; all films have similar elastic modulus values of approximately 125 GPa. The onset of microscale yielding has been identified using the bulge testing technique, and occurs at stresses approximately 50-70% of that which is expected from the hardness data, even when corrected for the localized stresses using estimations of the stress concentration based on a finite element analysis.

Though the CuNi films had poor adhesion, it was these films which were shown to withstand the highest stresses, reaching values approximately 1/3 higher than the CuNb and CuNbNi films. However, the CuNb films were shown to exhibit a higher hardness than the CuNi and CuNbNi films, atrend which for the CuNb and CuNi films has been shown by Misra et.al.[1,2] when comparing films of 10nm individual layer thickness. The samples which exhibit the highest hardness do not correspond to the highest initial yield strengths and as such future high cycle fatigue testing should be carried out at stresses low enough to minimize dislocation motion. These differences were attributed to a difference in the strain hardening abilities of these films.

Significant plastic deformation was shown in CuNb, CuNi and CuNbNi multilayers with strains greater than 5% achieved before failure. Mechanical Properties testing of elastic modulus, yield point, hardness and burst pressure led to the development of a predictive model for the stress strain behavior of CuNb, CuNi, and CuNbNi multilayers. Experimental stress strain curves have shown significant agreement with the model. The development in understanding the stress /strain behavior of these materials has led to identification of appropriate operating stresses for fatigue testing these multilayer thin film systems. While the CuNbNi Trilayer films did not show a significant improvement in the ultimate strength as compared to the CuNi films it should be noted that the benefit of these films over the CuNi system may lie in their ability to resist radiation damage, which is due to the incoherent CuNb interface not present in the CuNi film system. In addition, all the multilayer films of interest were shown to exhibit mechanical properties far surpassing that of the thin film gold.

Recommendations for future research on these film systems should include utilizing different indenter geometries in order to gain further information on the stress vs. strain relationships of these multilayers at higher strains. In addition, fabrication of rectangular window geometries with larger side lengths (short dimension greater than 2mm while maintaining an aspect ratio greater than four) should be incorporated. This improvement would allow for enhancement of the experiments by incorporating less noise in the deflection measurement at the higher pressures necessary for burst testing.

5.1 References

[1] Misra, A., Hirth, J.P., Hoagland, R.G., "Length-scale-dependent deformation mechanisms in incoherent metallic multilayered composites," (2005) Acta Mat. 53 pp.4817- 4824

[2] Zhang,X., Misra,A., Wang,H., Shen,T.D., Nastasi,M., Mitchell,T.E., Hirth,J.P., Hoagland, R.G., Embury,J.D., "Enhanced hardening in Cu/330 stainless steel multilayers by nanoscale twinning," (2004) Acta Mat. **52**(4), pp.995-1002

APPENDIX

A. Propagation of Error

The following is an analysis on the propagation of error in the bulge testing set-up. While different testing methods were found to be in agreement to within 10% when determining properties of the these films systems, a thorough understanding of the uncertainty in the test method should still be considered. For this analysis, the root sum squares (RSS) approach[1,2] was utilized for its ability to take into account variance of multiple measurements contributing to the calculation of a single parameter. For example, as stated in Chapter 2, the residual stress measured via the bulge test method is calculated as:

$$\sigma_o = \frac{A_{CurveFit} \cdot a^2}{C_1 \cdot t} \tag{A.1}$$

σ_o is the residual stress, $A_{CurveFit}$ is the linear term of the elastic pressure deflection curve fit, $C_1$is a geometric constant, "t" is the film thickness and "a" is one half of the membrane sidelength. Using the RSS approach, partial derivatives of σ_o with respect to each of the variables are taken and used to calculate the standard variation in the residual stress measurement ($S_{std\ \sigma o}$) as shown in Equation (A.2)

$$S_{std\ \sigma_o} = \sqrt{\left(\frac{\partial \sigma_o}{\partial A}\right)^2 s_A{}^2 + \left(\frac{\partial \sigma_o}{\partial a}\right)^2 s_a{}^2 + \left(\frac{\partial \sigma_o}{\partial t}\right)^2 s_t{}^2} \tag{A.2}^{1,2}$$

where "s" is the standard deviation[3] the individual measurements used when calculating the residual stress. The formula for calculation of the standard deviation is as follows.

$$s = \sqrt{\frac{1}{N} \cdot \sum_{i=1}^{\infty} (x_i - \bar{x})^2} \qquad \text{(A.3)}^3$$

With N equal to the number of samples, x corresponding to sample "i" and x-bar corresponding to the mean of samples "i" through infinity.

Table A1 shown below describes standard deviation values for several of the parameters measured throughout this thesis. The values shown are for sample sets of 5 square CuNb membranes and 5 rectangular CuNb membranes.

Table A.1 – Standard Deviation Values for square and rectangular membranes.

Measured Parameter	**Square (s)**	**Rectangle (s)**
Membrane Sidelength	.005mm	.0085 mm
Film Thickness (from LANL)	Unknown	Unknown
Curve Fit Parameter A	.053	.072
Curve Fit Paramter B	9.1*10^-6	9.74*10^-5
Poisson Ratio assumed = .25	0	0

While the standard deviation of the film thickness is not known because measurements were performed at Los Alamos National Labs, a value of .02μm was assumed for the deviation in this parameter.

Table A.2 – Propagated Error in Measurement

Film/Geometry/Property	**Value**	**Deviation (s)**	**% Error**
CuNb Square Modulus	124.8	13.97	11.2
CuNb Square Residual Stress	114.6	12.55	10.6
CuNb Rect. Modulus	117.8	16.72	14.2
CuNb Rect. Residual Stress	108.8	9.84	9.04

Analysis of the propagated error shown indicates that the square membranes are better suited for measurement of the modulus while the rectangular films are slightly

better suited for the residual stress measurement in these thin films. A potential reason for this could be due to the increased difficulty in alignment and measurement of the rectangular films due to their much smaller dimensions. As discussed in chapters four and five, it has been recommended that future bulge testing of thin film rectangular samples be carried out on larger rectangular substrates while also maintaining the current aspect ratio. In addition, the standard deviation of Poisson's ratio was assumed to be .25 for all the multilayer films. Because of this assumption, the standard deviation in this value was taken to be zero due to the fact that it did not contribute to the measurement error in the test method. However, it should be noted that the assumption of a .25 value for Poisson's ratio could result in a slight bias of the modulus and stress values which were calculated. For this reason, future recommendations also include the determination of Poisson's ratio for the film systems of interest.

References

[1] Author Unknown, "Cornell University, Propagation of Errors" Online Accessed, http://instruct1.cit.cornell.edu/courses/virtual_lab/LabZero/Propagation_of_Error.shtml

[2] Yeager, J.D., "Design and Development of Metal-Polymer Film Systems for Flexible Electrodes used in Cortical Mapping in Rats," M.S., Washington State University, 2008, USA.

[3] Montgomery, D.C., Runger, G.C., Hubele, N.F., "*Engineering Statistics*," Wiley, 2003, USA.